



HAL
open science

Variations in eastern Mediterranean hydrology during the last climatic cycle as inferred from neodymium isotopes in foraminifera

Maxence Duhamel, Christophe Colin, Marie Revel, Giuseppe Siani, Arnaud Dapoigny, Éric Douville, Jiawang Wu, Yulong Zhao, Zhifei Liu, Paolo Montagna

► To cite this version:

Maxence Duhamel, Christophe Colin, Marie Revel, Giuseppe Siani, Arnaud Dapoigny, et al.. Variations in eastern Mediterranean hydrology during the last climatic cycle as inferred from neodymium isotopes in foraminifera. *Quaternary Science Reviews*, 2020, 237, pp.106306. 10.1016/j.quascirev.2020.106306 . hal-02624107

HAL Id: hal-02624107

<https://hal.science/hal-02624107>

Submitted on 22 Aug 2022

HAL is a multi-disciplinary open access archive for the deposit and dissemination of scientific research documents, whether they are published or not. The documents may come from teaching and research institutions in France or abroad, or from public or private research centers.

L'archive ouverte pluridisciplinaire **HAL**, est destinée au dépôt et à la diffusion de documents scientifiques de niveau recherche, publiés ou non, émanant des établissements d'enseignement et de recherche français ou étrangers, des laboratoires publics ou privés.



Distributed under a Creative Commons Attribution - NonCommercial 4.0 International License

31 seawater ϵNd values observed during African Humid Periods (and sapropel events) are associated
32 with an intensification of Nile discharge and an increase in residence time of deep-water masses in
33 the eastern Mediterranean Sea, which induces an increase in the interaction between deep-water
34 masses and radiogenic sediments along the margin of the eastern Mediterranean Sea. Results
35 confirm that an intensification of the hydrological exchanges between the western and eastern
36 Mediterranean basins during high sea-level stand and the subsequent higher proportion of
37 Atlantic Water in the Levantine Basin may have preconditioned the eastern Mediterranean Sea to
38 sapropel depositions during the last climatic cycle.

39 **Key words:** *Neodymium isotopes; foraminifera; paleo-hydrology; sapropels; eastern*
40 *Mediterranean Sea; African monsoon.*

41

42 **1. Introduction**

43 The Mediterranean Sea is a semi-enclosed basin, where an excess of evaporation over
44 precipitation and runoff induces a characteristic eastward increase in the salinity of the surface
45 Atlantic water that enters through the Gibraltar Strait and flows to the eastern Mediterranean
46 basin; this water effectively becomes denser and contributes to the formation of intermediate and
47 deep waters. The resulting Mediterranean thermohaline circulation has been demonstrated to be
48 highly sensitive to present-day and past climate changes in both high and low latitudes (Rossignol-
49 Strick et al., 1982; Roether et al., 1996; Kallel et al., 1997; Pinardi and Masetti, 2000; Rohling et al.,
50 2002; Emeis et al., 2003; Scrivner et al., 2004; Melki et al., 2009; Revel et al., 2010; Toucanne et al.,
51 2015; Filippidi et al., 2016; Tesi et al., 2017). This variability is thought to be responsible for the
52 deposition of organic-rich sapropel layers (characterized by $>1\%$ C_{org}) in the Eastern
53 Mediterranean Sea (EMS) (Murat and Got, 2000) and of Organic Rich Levels (ORL) in the Western
54 Mediterranean Sea (WMS) (e.g. Rohling et al., 2015). However, paleo-hydrological processes and
55 associated ventilation dynamics related to sapropel deposition are still debated because
56 conventional water-mass proxies, such as $\delta^{13}\text{C}$ analyzed on benthic foraminifera, cannot be used
57 systematically due to the lack of benthic foraminifera in EMS sediments during time intervals
58 when bottom waters were characterized by anoxic conditions.

59 Despite many unresolved problems, such as the processes responsible for the sluggish
60 thermohaline circulation during deep-sea anoxic events, significant advances have been made

61 over recent decades in our understanding of sapropel formation since the pioneering work of
62 Rossignol-Strick et al. (1982). There is now a common consensus that the formation of sapropels in
63 the Mediterranean Sea is closely linked to: (1) reduced deep-water ventilation associated to
64 freshwater input lowering surface water salinity, thus causing stratification of the water masses
65 with limited or no oxygen renewal in deep water; or (2) nutrient-rich surface freshwater inputs,
66 which significantly increase surface productivity and induce the mineralization of organic matter in
67 deep water to a level that exceeds oxygen inputs through deep water mass renewal; or (3) a
68 combination of both processes (Rohling, 1994; Cramp and O'Sullivan, 1999; Rohling et al., 2015).
69 The leading role of stratification in most studied sapropels is revealed by the neodymium (Nd)
70 isotopic composition of biogenic/autogenic fractions (e.g. Freydier et al., 2001; Cornuault et al.,
71 2018; Wu et al., 2019), benthic foraminifera carbon isotopic records, faunal assemblages (e.g.
72 Kuhnt et al., 2008; Schmiedl et al., 2010; Cornuault et al., 2016), redox-sensitive elemental
73 compositions (e.g. Jilbert et al., 2010; Tachikawa et al., 2015; Tesi et al., 2017), and circulation
74 models (e.g. Myers et al., 1998; Myers, 2002; Stratford et al., 2000; Bianchi et al., 2006; Grimm et
75 al., 2015; Vadsaria et al., 2019).

76 Many studies have confirmed that periods of sapropel deposition are marked by high river runoff
77 originating from the low-latitude monsoonal system, whereas time intervals between sapropel
78 depositions are arid with reduced riverine runoff and increased wind-blown sediment supplies (e.g.
79 Wehausen and Brumsack, 1999; Larrasoana et al., 2003; Zhao et al., 2012; Revel et al., 2014). A
80 widely accepted explanation for the excess freshwater input during times of sapropel formation is
81 related to heavy monsoonal precipitation in North Africa which was channeled by the Nile River
82 and other North African paleo-rivers (e.g. Rossignol-Strick et al., 1982; Fontugne et al., 1994;
83 Rohling et al., 2002; Emeis et al., 2003; Scrivner et al., 2004; Osborne et al., 2008, 2010; Revel et
84 al., 2010; Wu et al., 2016, 2017). In North Africa, these humid periods have been attributed to the
85 northward migration of the rain belt associated with the Inter-Tropical Convergence Zone (ITCZ)
86 due to precession-driven insolation changes (Rossignol-Strick et al., 1982; DeMenocal et al., 2000;
87 Gasse, 2000; Arbuszewski et al., 2013; Skonieczny et al., 2015, 2019). The last period of more
88 intense rainfall compared to the present, the so-called African Humid Period (AHP: from ~14.8 and
89 ~6 cal kyr BP; Shanahan et al., 2015; Bastian et al., 2017), is thought to be responsible for the
90 formation of the organic-rich sapropel S1 in the EMS between 10.2 and 6.4 cal kyr BP (Mercone et
91 al., 2000; De Lange et al., 2008). Thus, the strong correspondence between sapropel formation
92 and periods of African monsoon intensification, when freshwater discharge by North African rivers

93 into the Mediterranean Sea increased, suggests that the reduction in sea surface salinity and
94 deep-water convection could be the result of changes in the African monsoon system (Revel et al.,
95 2015; Rohling et al., 2015). However, enhanced freshwater inputs from the northern margin of the
96 Mediterranean Sea related to precipitations driven by westerly winds and the melting of glacial
97 ice-sheets and linked to climate changes in the high latitudes of the Northern hemisphere (e.g.
98 Kallel et al., 1997; Emeis et al., 2003; Melki et al., 2009; Toucanne et al., 2015; Filippidi et al., 2016;
99 Tesi et al., 2017) would have also led to the reduction of deep-water formation in the EMS,
100 limiting the oxygen supply to the deep water (Rohling, 1994). Furthermore, several studies have
101 shown that the Mediterranean thermohaline circulation is sensitive to rapid climatic changes in
102 the northern hemisphere (e.g. Heinrich and Dansgaard - Oeschger events) (Rohling et al., 1995;
103 Kallel et al., 1997; Allen et al., 1999; Bartov et al., 2003; Martrat et al., 2004).

104 In addition, the narrow and shallow Siculo-Tunisian and Gibraltar Straits tend to limit exchanges
105 between the eastern and western Mediterranean basins, and with the North Atlantic. It has been
106 proposed that water exchanges through the Straits may have been significantly limited during the
107 glacial low sea-level stands of the late Quaternary. A general circulation model has shown that
108 Mediterranean water outflow was reduced by 50% during the Last Glacial Maximum (LGM)
109 (Mikolajewicz, 2011), and several studies have pointed to a salinity increase in the eastern basin
110 (Thunell and Williams, 1989; Myers et al., 1998a). In particular, Mikolajewicz (2011) has shown
111 that the formation of deep waters in the eastern basin during the LGM was strengthened and that
112 these waters were principally formed in the Aegean Sea and not in the Adriatic Sea as is the case
113 today. It has also been proposed that rising global sea level during deglaciation led to greater
114 exchanges between the basins and a drop in surface salinity, thus preconditioning the sapropel
115 event by slowing down intermediate and deep convections (Grimm et al., 2015).

116 Studies of past changes in Mediterranean thermohaline circulation have mostly investigated the
117 last glacial period, focusing on the deposition of sapropel S1 (10.2 – 6.4 cal kyr BP; Mercone et al.,
118 2000) (e.g. Cacho et al., 2002; Sierro et al., 2005; Frigola et al., 2008; Schmiedl et al., 2010;
119 Toucanne et al., 2012; Angue Minto'o et al., 2015; Jiménez-Espejo et al., 2015). Continuous $\delta^{13}\text{C}$
120 and $\delta^{18}\text{O}$ records from epibenthic foraminifera of the last glacial – interglacial climatic cycle are
121 rare and difficult to obtain for bottom suboxic or anoxic environments (e.g. sapropel events) in the
122 EMS. This is due to the lack of a continuous population of epibenthic foraminifera species for
123 which a calibrated vital effect for $\delta^{13}\text{C}$ analyses is well established (Schmiedl et al., 2003, 2010).

124 Consequently, the hydrological pattern of the EMS is not well constrained for periods of sapropel
125 deposition and for the time intervals that preconditioned such events.

126 In the present study, we have investigated the Nd isotopic composition (ϵNd) of the diagenetic Fe-
127 Mn coatings precipitated on foraminifera shells. It has been demonstrated that ϵNd measured on
128 planktonic foraminifera shells represents mainly bottom seawater and/or pore water ϵNd
129 (Tachikawa et al., 2013, 2014). Such ϵNd obtained from foraminiferal shells have been previously
130 used to provide information on water mass provenance and mixing in the ocean (Molina-Kescher
131 et al., 2014; Wu et al., 2015b, 2019; Dubois-Dauphin et al., 2017; Cornuault et al., 2018). Modern
132 Mediterranean seawater displays a wide range of ϵNd values, from -11 to -5, with unradiogenic
133 surface water entering the Mediterranean as Atlantic Water and more radiogenic intermediate
134 and deep waters originating from the Levantine Basin (Henry et al., 1994; Tachikawa et al., 2004;
135 Vance et al., 2004). With a residence time of 500-1000 years (Tachikawa et al., 2003; Siddall et al.,
136 2008) and distinct local basin-scale sources, ϵNd is assumed to behave quasi-conservatively, with
137 great potential to fingerprint the provenance of Mediterranean water masses (Dubois-Dauphin et
138 al., 2017; Cornuault et al., 2018; Wu et al., 2019).

139 The ϵNd of mixed planktonic foraminifera from two sediment cores collected in the Levantine
140 Basin were investigated in order to reconstruct past ϵNd of the EMDW over the last 145 kyr.
141 Combined with previous ϵNd records, the new results allow us to assess the relative contributions
142 of Nile discharge and inflow of Modified Atlantic Water (MAW) to the thermohaline circulation of
143 the EMS over the last climatic cycle characterized by several anoxic events and the deposition of
144 sapropels S1 to S5. This allows us to constrain the hydrology at the origin of these anoxic events
145 under different environmental conditions (different sea levels, different freshwater supplies from
146 the African rivers and different hydrological exchange conditions at the Gibraltar and the Siculo-
147 Tunisian Straits).

148 **2. Regional hydrological setting in terms of ϵNd**

149 The Mediterranean Sea is an almost enclosed basin that exchanges surface and intermediate
150 waters with the Atlantic Ocean through the Gibraltar Strait (sill depth ~ 300 m) and surface water
151 with the Black Sea through the Dardanelles Strait (sill depth ~ 100 m). Driven by a negative water
152 budget, an anti-estuarine circulation occurs in the Mediterranean Sea. Hence, the relatively fresh
153 surface Atlantic Water (AW) (salinity ~ 36.5), which has an unradiogenic ϵNd signature of ~ -9.7
154 (Tachikawa et al., 2004), flows into the WMS and is then modified by mixing with the ambient

155 surface water to reach ~ -10.4 in the Alboran Sea (Tachikawa et al., 2004, Spivack and Wasserburg,
156 1988). During its eastward flow, AW mixes with the surrounding surface waters and underlying
157 intermediate waters leading to the formation of the Modified Atlantic Water (MAW) that flows
158 along the basin at 50-200 m water depth following a general cyclonic flow path with several eddies
159 and meanders (Fig. 1). The ϵNd values for MAW range from -10.8 to -9.0 in the western basin
160 (Henry et al., 1994) and from -9.8 to -4.9 in the eastern basin (Tachikawa et al., 2004; Vance et al.,
161 2004). Since evaporation exceeds precipitation and river runoff, the relatively fresh surface AW
162 flowing into the WMS also becomes progressively saltier (~ 38.5) as it circulates eastward.

163 During winter time, intense cooling and strong wind-induced heat loss produce denser waters that
164 sink via convection and form the intermediate waters in the Aegean Sea and the Levantine Basin
165 and deep waters in the Gulf of Lions and the Adriatic Sea (Robinson et al., 2001; Schroeder et al.,
166 2012). In particular, the Levantine Intermediate Water (LIW) is formed in the Cyprus-Rhodes area
167 and it spreads westwards throughout the entire Mediterranean Basin at depths of between ~ 150 -
168 700 m (Lascaratos et al., 1993; Malanotte-Rizzoli et al., 1999). The LIW acquires its ϵNd signature
169 mainly from the partial dissolution of particles from the Nile River and the Egyptian/Libyan margin
170 sediments of the EMS, which have ϵNd values ranging from -7 to -2 (Weldeab et al., 2002a;
171 Tachikawa et al., 2004; Ayache et al., 2016). This more radiogenic Nd signature is explained by
172 sediment originating from the erosion of Ethiopian traps including Cenozoic basaltic silicate rocks
173 ($\epsilon\text{Nd} > 0$) (Garzanti et al., 2015). The LIW is thus characterized by a radiogenic ϵNd of ~ -4.8 in the
174 eastern part of the EMS and by an east-west ϵNd gradient ranging from -4.8 to -9.2, resulting from
175 mixing with overlying and underlying water masses along its path (Henry et al., 1994; Tachikawa et
176 al., 2004; Vance et al., 2004). In the Adriatic Sea, LIW is involved in the formation of Adriatic Deep
177 Water (AdDW) that sinks into the deep EMS contributing, together with the Aegean Deep Water
178 (AeDW), to the formation of the Eastern Mediterranean Deep Water (EMDW). The EMDW ϵNd
179 values range from -7 to -6 with an average value of -6.5 (Tachikawa et al., 2004). The Western
180 Mediterranean Deep Water (WMDW) is formed in the Gulf of Lions in winter, as a result of mixing
181 between the relatively fresh surface water and the saline LIW; it then spreads into the Balearic
182 Basin and Tyrrhenian Sea between ~ 2000 and ~ 3000 m (Millot, 1999; Schroeder et al., 2012) (Fig.
183 1). The WMDW is characterized by an average ϵNd value of -9.4 ± 0.9 (Henry et al., 1994;
184 Tachikawa et al., 2004). Between the WDMW and the LIW (from ~ 700 to ~ 2000 m), the
185 Tyrrhenian Deep Water (TDW) (Millot et al., 2006), which is produced by mixing between WMDW
186 and EMDW, has an average ϵNd value of -8.1 ± 0.5 .

187 The Blue Nile and Atbara rivers represent together 97% of the suspended sediment load and 68%
188 of the freshwater supply of the total annual Nile discharge (Foucault and Stanley, 1989; Williams
189 et al., 2000; Revel et al., 2015). ϵNd signatures of sediments from the Nile Basin are characterized
190 by contrasted signatures, ranging from radiogenic values ($\epsilon\text{Nd} \approx 0$) for the Cenozoic Ethiopian
191 traps to strongly unradiogenic values ($\epsilon\text{Nd} \approx -30$) for the Precambrian Central Africa Craton
192 (Garzanti et al., 2015). Sediments from the Bahr el Jebel (between Lake Albert and 10°N of
193 latitude) are characterized by a ϵNd value of -25, whereas Victoria-Albert Nile-derived fluvial
194 muds by a range from -29 to -36 (Padoan et al., 2011). The Equatorial-White Nile sediment
195 makes up approximately 3.5 % of the present-day total sediment discharge of the Nile and is fairly
196 constant throughout the year (Blanchet et al., 2015; Garzanti et al., 2015), with a very
197 unradiogenic signature (from -30 to -35). In contrast, the Blue Nile sediment, which is mainly
198 transported during the humid phase, dominates the total sediment discharge of the Nile (72%)
199 and is characterized by very radiogenic ϵNd values (from -3 to 5; Padoan et al., 2011; Blanchet et
200 al., 2013; Garzanti et al., 2015).

201 **2. Material and methods**

202 **2.1 Studied cores**

203 For this study, we have selected cores MD90-964 and MS27PT, which are bathed by the Eastern
204 Mediterranean Deep Water (EMDW).

205 Core MD90-964 (33°02.75'N, 32°38.57'E; water depth 1375 m, length 32.12 m) was collected on
206 the eastern part of the Nile deep-sea fan during the PROMETE III campaign on board R/V Marion
207 Dufresne in September 1990 (Fig. 1). Core MD90-964 sediments consist of pale cream to yellowish
208 brown foraminiferal and nannofossil marl ooze, interbedded with sapropelic layers that vary in
209 thickness from 2 to 41 cm (Zhao et al., 2011). The $\delta^{18}\text{O}$ of *Globigerinoides ruber*, clay mineralogy,
210 total organic carbon (TOC) content and elemental intensities by X-ray fluorescence (XRF) have
211 been studied previously by Zhao et al. (2011). The age model of core MD90-964 (Zhao et al., 2011)
212 has been established by correlating the *G. ruber* $\delta^{18}\text{O}$ record and the Mediterranean *G. ruber* stack
213 compiled by Lourens (2004), using Gaussian filtering at both obliquity and precession, and cross-
214 spectral analysis against a target curve that reflects characteristics of orbital parameters (ETP
215 curve). According to the age model, the upper 7.30 m of core MD90-964 investigated in this study
216 cover the last 145 kyr and present a linear mean sedimentation rate of 5 cm/kyr. Sapropels S1, S3,

217 S4 and S5 are identified by an increase of C_{org} content, which reaches up to 6 % during the
218 deposition of sapropel S5 (Fig. 2; Zhao et al., 2011).

219 Core MS27PT (31°47.90'N, 29°27.70'E; water depth 1389 m, length 7.3 m) was retrieved on the
220 western Nile delta, around 90 km from the mouth of the Rosetta Nile River, during the Mediflux
221 MIMES cruise of the R/V Pelagia in 2004 (Fig. 1). The core site lies directly under the influence of
222 the Nile freshwater discharge. For this study, we have investigated the upper 3.15 m of core
223 MS27PT which consist of carbonate-rich facies with coarse quartz grains and clastic mud-rich
224 facies where sapropel S1 has been identified (Revel et al., 2010) (Fig. 2). The age model of the
225 studied interval of core MS27PT is based on 22 previously published AMS ^{14}C dates (Revel et al.,
226 2010, 2015; Bastian et al., 2017; Menot et al., 2020) (Fig. 2).

227 **3. Methods**

228 The samples investigated in this study consist of 15 to 30 mg of mono-specific planktonic
229 foraminifera *G. ruber* and mixed planktonic foraminifera, hand-picked in the >150 μm size fraction.
230 Cleaning procedure and purification of Nd have been done in a class 100 clean laboratory using
231 ultrapure reagents. All of the test samples were crushed between two glass slides to open the
232 foraminiferal chambers. The calcite fragments were then ultrasonicated for 1 min before pipetting
233 off the suspended particles with water to separate the waste. This step was repeated until the
234 water became clear and free of clay. All samples were checked under a binocular microscope to
235 ensure that all particles had been removed. Most of the samples were then analyzed after this
236 preliminary physical cleaning step (hereafter referred as “uncleaned foraminifera”) (Wu et al.,
237 2015b).

238 For this study, some physically cleaned samples were transferred to centrifuge tubes for an
239 oxidative-reductive cleaning step (hereafter referred as “cleaned foraminifera”). The oxidative-
240 reductive foraminiferal cleaning procedure followed that described by Vance and Burton (1999),
241 using 10 ml reductive solution (1 M hydrous hydrazine, 16 M NH_4OH , 0.25 M citric acid in a ratio of
242 1:6:3) and 5 ml oxidative solution (0.2 M NaOH and 30% H_2O_2 in a 1:1 ratio) per sample to more
243 efficiently remove authigenic Fe-Mn coatings and organic material. For the reductive step,
244 samples were heated in a water bath at 80°C for 30 min, and were ultrasonicated every 3 min for
245 10 s. After transferring the reductive cleaning solution to a centrifuge tube, the cleaned
246 foraminifera were rinsed with Milli-Q water. The analytical procedure for the oxidative step was
247 similar except that samples were ultrasonicated every 10 min for a period of 30 s.

248 All samples, including uncleaned foraminifera, underwent weak acid leaching for 5 min in 1 ml
249 0.001 M HNO₃ with ultrasonication. After these cleaning steps, samples were transferred into a
250 1.5 ml tube. 0.5 ml of Milli-Q water was first added to the tube, and then the foraminifera were
251 dissolved using stepwise 100 µl 0.5 M HNO₃ until the dissolution reaction stopped. The dissolved
252 samples were centrifuged, and the supernatant was immediately transferred to Teflon beakers to
253 prevent leaching of any possible remaining phases. The dissolved foraminifera shell fractions and
254 authigenic fractions contained in the reductive cleaning solution were dried using a hotplate for
255 Nd extraction. Nd was purified using Eichrom TRU-Spec and Ln-Spec resins following the detailed
256 analytical procedures described in Copard et al. (2010). The ¹⁴³Nd/¹⁴⁴Nd ratios were measured
257 using the ThermoScientific Neptune^{Plus} Multi-Collector Inductively Coupled Plasma Mass
258 Spectrometer (MC-ICP-MS), hosted at the Laboratoire des Sciences du Climat et de
259 l'Environnement (LSCE) in Gif-sur-Yvette. For the Nd isotope analyses, sample and standard
260 concentrations were matched at 10 ppb. Mass-dependent fractionation was corrected by
261 normalizing ¹⁴⁶Nd/¹⁴⁴Nd to 0.7219 and applying an exponential law. During the analytical sessions,
262 every set of two samples was bracketed by analyses of the La Jolla Nd standard solution, which is
263 characterized by certified values of 0.511858±0.000007 (Lugmair et al., 1983). The offset value
264 between results and certified values of La Jolla standard was lower than 0.4 epsilon units (εNd) for
265 all of the analyses presented in this study. The analytical errors reported herein correspond to the
266 external 2 sigma standard deviation (based on repeated analyses of the La Jolla standard for the
267 different analytical sessions) and range from 0.1 to 0.5 εNd (Table 1 and Table 2). The analytical
268 blank values for Nd evaluated by using a quadrupole ICPMS were <4 pg, which represents less
269 than 0.1% of the minimum Nd yield from foraminifera used in this study. As a result, no blank
270 correction was applied. Results are expressed as εNd = [(¹⁴³Nd/¹⁴⁴Nd)_{sample}/(¹⁴³Nd/¹⁴⁴Nd)_{CHUR} - 1]
271 *10000, with the present-day (¹⁴³Nd/¹⁴⁴Nd)_{CHUR} of 0.512638 (Jacobsen and Wasserburg, 1980).

272 **4. Results**

273 **4.1 The εNd record of cores MS27PT and MD90-964**

274 The εNd values from core MS27PT, obtained on both monospecific samples of planktonic
275 foraminifer *G. ruber* and mixed planktonic foraminifera, exhibit a wide range from -5.71±0.13 to -
276 2.51±0.21 (Table 1 and Fig. 3). The εNd values of monospecific and mixed samples from the same
277 sediment volume are in agreement within an uncertainty of 2 sigma (Table 1). It is worth noting
278 that mean εNd values obtained from foraminifera cleaning solutions are similar or slightly more

279 radiogenic than cleaned foraminifera. This confirms that oxidative-reductive cleaning procedures
280 applied to foraminiferal tests from our sampling sites are not effective to fully remove the Nd
281 associated with the authigenic Fe-Mn coating (Wu et al., 2015b). Therefore, ϵNd obtained in both
282 reductively cleaned and non-reductively cleaned foraminifera are associated with bottom and/or
283 pore-water ϵNd values as it has been demonstrated elsewhere for a large compilation of ϵNd
284 results obtained from foraminifera (Tachikawa et al., 2014).

285 For core MS27PT, ϵNd displays lower values of -4.7 ± 0.2 to -4.9 ± 0.1 between 21 and 16.4 cal kyr BP
286 (Fig. 3). It increases to more radiogenic values (-2.5 ± 0.2 to -4.4 ± 0.3) in the time interval between
287 14.1 and 6.8 cal kyr BP, corresponding to the AHP which is associated with higher Nile flood
288 discharges (DeMenocal et al., 2000; Revel et al., 2015; Castañeda et al., 2016). The highest value
289 (-2.5 ± 0.2) is recorded at 9.7 cal kyr BP. The ϵNd values then steadily decrease from -2.5 ± 0.2 to
290 -5.5 ± 0.3 between 9.7 and 4.3 cal kyr BP. The time interval coeval with the period during which
291 sapropel S1 was deposited (10.2-6.4 cal kyr BP) is associated with radiogenic ϵNd values (from
292 -2.7 ± 0.2 to -4.3 ± 0.2). The time interval between 4.3 and 1.5 cal kyr BP presents unradiogenic ϵNd
293 values (up to -5.9 ± 0.1) which increase again thereafter to reach -4.0 ± 0.1 at the core top.

294 For core MD90-964, ϵNd values were obtained for samples of uncleaned mixed foraminifera from
295 the Marine Isotope Stage (MIS) 6 to the Holocene (Fig. 4E). In general, glacial MIS6, MIS4, MIS3
296 and MIS2 are characterized by high ϵNd values, ranging from -3.8 ± 0.2 to -2.8 ± 0.2 . In contrast,
297 interglacial MIS5 and the Late Holocene display lower ϵNd values, from -4.5 ± 0.2 to -2.8 ± 0.3 .
298 Superimposed on this long-term glacial-interglacial variation, the monsoon-precession induced
299 signal is distinguished by more radiogenic values related to the African Humid Periods (from 123.5
300 to 121.7 cal kyr BP, 102.3 to 99.3 cal kyr BP, 84.3 to 81.8 cal kyr BP; 55 cal kyr BP and 9.5 to 6.2 cal
301 kyr BP) (e.g. Gasse, 2000; Zhao et al., 2012). These time intervals are also associated with an
302 increase of C_{org} in core MD90-964 and are coeval with the deposition of sapropels S5 (128.0 to
303 117.7 cal kyr BP), S4 (102.3 to 100.6 cal kyr BP), S3 (81.8 to 79.7 cal kyr BP) and S1 (10.1 to 5.7 cal
304 kyr BP) (Fig. 4F) (Zhao et al., 2011). In particular, ϵNd values systematically increase before the
305 deposition of sapropels S4, S3 and S1.

306 For the last 20 cal kyr BP, the ϵNd record obtained on core MD90-964 displays long-term
307 variations that are consistent with those of core MS27PT. Interestingly, higher ϵNd values from
308 ~ 14 to ~ 6 cal kyr BP are coeval with the timing of the AHP (Fig. 3). The time interval between 9 and
309 6 cal kyr BP is marked by a steady decrease of ϵNd during the Late Holocene (Fig. 3), whereas the

310 interval between 4 and about 1.5 cal kyr BP displays lower values before they increase again
311 during the last 1.5 cal kyr BP.

312 **4.2 Regional compilation of seawater ϵ Nd of the Levantine Basin**

313 Previous studies of the Nd isotopic compositions of authigenic oxy-hydroxides in the Levantine
314 Basin have been conducted on leached bulk sediment (Freydier et al., 2001; Cornuault et al., 2018;
315 Wu et al., 2019), fish debris/teeth (Wu et al., 2019) and on planktonic foraminifera (Scrivner et al.,
316 2004; Vance et al., 2004; Osborne et al., 2010; Cornuault et al., 2018; Wu et al., 2019). Past
317 seawater ϵ Nd has been obtained from bulk sediment leachates using different analytical
318 procedures such as bulk sediment leached with 1 M HCl (Freydier et al., 2001; Wu et al., 2019) and
319 hydroxylamine hydrochloride of non-decarbonated samples (Tachikawa et al., 2004; Cornuault et
320 al., 2018). ϵ Nd analyses of foraminifera have previously been conducted on both uncleaned
321 foraminifera (Cornuault et al., 2018) and samples treated with an oxidative-reductive leaching
322 procedure (Scrivner et al., 2004; Vance et al., 2004; Osborne et al., 2010). All of these analytical
323 procedures have been debated within the scientific community and have been deemed suitable
324 for extracting the ϵ Nd signature of the deep-water masses of the ocean.

325 Previous ϵ Nd records based on cleaned foraminifera collected in the eastern Levantine Basin (ODP
326 Site 967C - 34°04.270'N; 32°43.528'E; 2552.8 m; Scrivner et al., 2004), in the western Levantine
327 Basin (OPD Site 971A - 33°42.818'N; 24°42.108'E; 2140.9 m; Osborne et al., 2008) and in the
328 south-eastern Aegean Sea (core LC21 - 35°39.7'N; 26°35.0'E; 1520 m; Osborne et al., 2010) were
329 used to reconstruct past ϵ Nd of surface waters. However, it has been recently demonstrated that
330 ϵ Nd of fossil planktonic foraminifera is not related to the ambient seawater at calcification depths,
331 but instead reflects bottom and/or pore-water ϵ Nd values due to the presence of residual
332 authigenic Fe-Mn coatings precipitated onto the carbonate shells that cannot be removed by
333 chemical cleaning procedures (Piotrowski et al., 2012; Roberts et al., 2012; Wu et al., 2015b; Xu et
334 al., 2018). ϵ Nd results obtained from cleaned foraminifera of core LC21 and ODP sites 967C and
335 971A should be interpreted as bottom/pore water ϵ Nd.

336 ODP Site 967C is also located within the EMDW (2551 m) and about 100 km away from core
337 MD90-964 making it possible to directly compare their ϵ Nd records for time intervals
338 corresponding to sapropels S1 and S5 (Figs. 5 and 6). ϵ Nd records for core MD90-964 and Site
339 967C, display more radiogenic values during African Humid Periods than before and after these
340 time intervals. For core MD90-964, the highest ϵ Nd value is observed in the early African Humid

341 Period (at 13.2 cal kyr BP) before the deposition of sapropels S1. Except this highest ϵNd value,
342 both sapropels of core MD90-964 (S5 and S1) display a range from -3.5 ± 0.2 to -4.8 ± 0.2 ,
343 characterized by slightly more radiogenic values compared to those obtained in the ODP Site 967C
344 (-5.5 ± 0.5 to -3.1 ± 0.2 ; Scrivner et al., 2004).

345 For the last 20 cal kyr BP, core MS27PT is also characterized by similar long-term variations of ϵNd
346 with an interval of more radiogenic values between 14 and 6 cal kyr BP followed by a progressive
347 return to unradiogenic values from 6 to 4 cal kyr BP. For cores MS27PT and MD90-964, the last
348 about 1.5 cal kyr BP show more radiogenic values. The good agreement observed in the long-term
349 changes of the ϵNd during the S5 (for core MD909-964 and ODP Site 967C) and the last 18 cal kyr
350 BP (for core MS27PT, core MD909-964 and ODP Site 967) suggests that all these cores provide a
351 regional Nd isotopic signature of the EMDW.

352 Core MD04-2722 located south of Cyprus at 1780 m water depth in the eastern Levantine Basin
353 (Fig. 1) presents radiogenic LGM ϵNd values (around -3), comparable to those observed for cores
354 located along the Nile deep-sea fan. ϵNd values decrease between 17.5 and 15 cal kyr BP followed
355 by a time interval characterized by radiogenic isotopic composition between 14.5 and 5 cal kyr BP
356 (Fig. 5). The time interval thereafter (between 5 and 3 cal kyr BP) is associated with a slight
357 decrease in the ϵNd values. Such long-term variations in ϵNd are quite similar to those observed in
358 cores MD90-964 and MSPT27 located upstream of the general counterclockwise deep-sea
359 circulation of the eastern Mediterranean basin (Fig. 1). Superimposed on this long-term trend,
360 core MD04-2722 is characterized by shifts of ϵNd to unradiogenic values around 13.5 and 6.8 cal
361 kyr BP that are not observed in other ϵNd records of the Levantine Basin (MD90-964, MS27PT and
362 ODP Site 967C), with the exception of one shift to a single unradiogenic value at 6.8 cal kyr BP
363 which is also observed in the ODP Site 967C (Fig. 5). This may reflect different time resolutions or a
364 potential local effect on Nd isotopic signature. This implies that long-term variations of ϵNd below
365 approximately 1300 m water depth reflect a regional ϵNd signal of the Levantine Basin. We note
366 a slight decrease of the ϵNd range along the north-eastward circulation pattern of the deep-water
367 masses that could be the result of a slight modification of the Nd isotopic signature of deep-water
368 masses through lithogenic Nd input from the volcanic margin of the eastern Levantine Basin.

369 In contrast, the ϵNd record of core BC07, located closer to core MD90-964 and at shallower depth
370 (893 m), displays variations from -6.2 ± 0.3 to -4.2 ± 0.3 (Freydier et al., 2001) that differ somewhat
371 from those of ODP Site 967C and core MD90-964 during the AHP (Fig. 5). While time intervals

372 before 15 cal kyr BP and after 6 cal kyr BP are characterized by similar ϵNd variations as ODP Site
373 967C and cores MD90-964 and MS27PT, the AHP is instead associated with more unradiogenic
374 ϵNd , with values as low as -5.9 ± 0.3 during the sapropel S1. This suggests that the ϵNd record of
375 water masses at ~ 900 m differs from those obtained at greater water depths (below ~ 1300 m) for
376 a time interval between 14 and 6 cal kyr BP. The difference between ϵNd records above and below
377 ~ 1300 m reaches its maximum during the time interval of sapropel S1 deposition.

378 **5. Discussion**

379 The ϵNd record obtained from uncleaned foraminifera of core MD90-964 allows us to establish,
380 for the first time, the Nd isotopic signature of the EMDW of the Levantine Basin over the last
381 climatic cycle and to extend our knowledge of the ϵNd variability for sapropels S1 and S5 to those
382 of S3 and S4. The ϵNd record of core MD90-964 also displays glacial-interglacial variability with
383 more radiogenic values during glacial MIS (Fig. 4).

384 A prerequisite for interpreting such seawater ϵNd variations through time is the characterization
385 of present-day Nd isotopic composition of the main water masses circulating in the eastern
386 Mediterranean basin. Thus, we can evaluate potential temporal changes in the ϵNd of the end-
387 members during the last climatic cycle, and assess the potential influences of lithogenic Nd input
388 and regional “boundary exchange” on ϵNd of deep-water masses.

389 **5.1 Possible impact of changes in lithogenic Nd input on the ϵNd of the Eastern** 390 **Mediterranean Deep Water in the Levantine Basin**

391 At the present time, the EMS is characterized by contrasting seawater ϵNd values (~ -10 to -5) with
392 strong zonal and vertical gradients which are attributed to a mixing between the inflowing MAW
393 (~ -10) and the more radiogenic underlying LIW (~ -5) and EMDW (~ -6.5) (Tachikawa et al., 2004)
394 (Fig 1b). The latter acquires its ϵNd signature from boundary exchange with radiogenic basaltic
395 material originating from the Ethiopian traps, which is transported to the EMS by the Nile river
396 ($\epsilon\text{Nd} = -3$ to $+3$, Tachikawa et al., 2004), and from the volcanic arc of the Aegean Sea ($\epsilon\text{Nd} \sim -2.5$),
397 with the most radiogenic material being located at the eastern border of the Levantine Basin (ϵNd
398 $= +3.5$ to $+6$) (Ayache et al., 2016).

399 In this regard, previous studies have explored past variations of seawater ϵNd in the Levantine
400 Basin as a balance between unradiogenic aeolian Saharan dust and radiogenic Nile river discharge
401 (Scrivner et al., 2004; Revel et al., 2015; Cornuault et al., 2018; Wu et al., 2019), including the

402 possibility of a significant contribution from paleo-rivers along the African margin (Osborne et al.,
403 2010), or a predominant contribution through the mechanism of boundary exchange (Ayache et
404 al., 2016; Vadsaria et al., 2019; Wu et al., 2016). Tachikawa et al. (2004) have suggested that the
405 Nd flux from Nile River freshwater has a minor influence on the present-day Mediterranean
406 seawater ϵNd , with its Nd concentration being low and the water input 10 times smaller than the
407 unradiogenic AW flowing from the Western Basin to the shallow waters of the Levantine Basin.
408 Several previous studies have demonstrated that detrital material in the Nile deep-sea fan results
409 from the mixing of sediments derived from Saharan/Libyan dusts and Nile sediments (Weldeab et
410 al., 2002a; Scheuvens et al., 2013; Garzanti et al., 2015; Revel et al., 2015). Cores MD90-964 and
411 MS27PT, located on the Nile deep-sea fan, are then suitable for assessing lithogenic Nd input to
412 the EMDW.

413 **5.1.1 Contribution of the Nile river**

414 Past humid periods, corresponding to the sapropels, were systematically accompanied by higher
415 deposition of iron/smectite-rich sediments in the Nile deep-sea fan, reflecting enhanced physical
416 erosion and transport of sediments from the Ethiopian Highlands (Krom et al., 1999, 2002;
417 Weldeab et al., 2002b; Revel et al., 2010, 2014, 2015; Langgut et al., 2011; Zhao et al., 2012). In
418 contrast, past arid periods are associated with a lower contribution from the Blue Nile and a
419 higher relative proportion of sediments derived from the White Nile, along with a peak in the
420 aeolian dust component (Revel et al., 2015; Zhao et al., 2012). Large smectite contents recorded in
421 cores MD90-964 (Zhao et al., 2012) (Fig. 4D) and MS27PT, combined with Sr and Nd isotopic
422 compositions (Revel et al., 2014) indicate the dominant contribution of the Blue Nile (smectite) to
423 the Nile discharge, at least during the last climatic cycles. The low proportion of sediment derived
424 from the White Nile is mainly due to the Sudd marshes in Southern Sudan which efficiently trap
425 sediments from tributaries of the White Nile (Padoan et al., 2011; Garzanti et al., 2015). In
426 addition, during the African Humid Periods, it has been suggested that large lakes formed in the
427 region extending from Sudd to the confluence at Khartoum (Barrows et al., 2014). These lakes
428 likely further limited the northward transport of unradiogenic Nd sediments to the Nile deep-sea
429 fan. Thus, there is no argument to support the hypothesis that changes in the relative contribution
430 of the Equatorial-White Nile and Blue Nile tributaries triggered the seawater ϵNd variations
431 observed in cores MD90-964 and MSPT27.

432 **5.1.2 Contribution of African dust**

433 The Saharan dust transported to the EMS is characterized by an unradiogenic ϵNd values (-15 to -
434 11; Padoan et al., 2011; Scheuvens et al., 2013), potentially contributing to the unradiogenic Nd
435 isotopic signature of surface and intermediate water masses (e.g. Tachikawa et al 2004; Ayache et
436 al., 2016). However, the present-day distribution of ϵNd in the surface and intermediate water
437 masses of the Mediterranean Sea is mainly attributed to the mixing of the AW and the LIW and
438 suggests a negligible contribution of Nd lithogenic input from aeolian dusts (Wu et al., 2019).

439 In addition, core MD90-964, located at a distal position on the deep-sea fan, is characterized by
440 lower mean sedimentation rates (5 cm/kyr) compared to core MS27PT (12 cm/kyr) and may be
441 associated with a higher proportion of Saharan dust components. Variations in the mineralogical
442 ratio of smectite/illite obtained on the clay fraction of core MD90-964 have been used to track the
443 relative proportions of Saharan dust (characterized by high illite contents) and Nile contributions
444 (dominated by smectite, 90%, derived from the Blue Nile and Atbara River draining the Ethiopian
445 Plateau flood basalts) (Zhao et al., 2011) (Fig. 4D). The transport of Saharan dust to the Levantine
446 Basin, reconstructed from the smectite/illite ratio, displays slight glacial-interglacial variations with
447 elevated dust inputs during glacial periods. Such results are in agreement with previous studies
448 reporting an increase in dust input to the Mediterranean Sea during this time span induced by the
449 southward migration of the ITCZ (Weldeab et al., 2002b; Revel et al., 2010; Ehrmann et al., 2016,
450 2017; Lamb et al., 2018) (Fig. 4D). Such glacial increases of unradiogenic ϵNd dust inputs to the
451 eastern Mediterranean Basin do not appear to have significantly modified the seawater ϵNd
452 record obtained in core MD90-964, since glacial periods (MIS6 and MIS2-4) are systematically
453 associated with more radiogenic ϵNd values than those of interglacial periods (MIS5 and MIS1)
454 (Figs. 4D and 4E).

455 In addition, the seawater ϵNd record obtained in core BC07, which was collected at a shallower
456 depth (893 m), could have been slightly more affected by the dissolution of Saharan dust relative
457 to the other deeper cores. Such higher contribution of dust dissolution in the upper water column
458 has been demonstrated in previous studies (e.g. Ayache et al., 2016). Yet, this core does not
459 exhibit variations in seawater ϵNd that might have been induced by a glacial increase in dust fluxes.
460 The time interval corresponding to the AHP (from ~ 14.8 and ~ 6 cal kyr BP), when a decrease of
461 aeolian dusts has been demonstrated (DeMenocal et al., 2000; Ehrmann et al., 2013), is in fact
462 associated with more unradiogenic ϵNd (Fig. 5). A negligible contribution of the dissolution of
463 African dust on past seawater ϵNd since the last glacial period has been also proposed by

464 Cornuault et al. (2018) and Wu et al. (2019) for several seawater ϵNd records obtained from cores
465 located between ~ 800 and ~ 3400 m water depth in the western part of the EMS.

466 **5.1.3 Contribution of African paleo-rivers**

467 A vast fossil river channel network has been identified in the Libyan Sahara, which was active
468 during African Humid Periods (Rohling et al., 2002). These paleo-rivers carried alteration products
469 originating from basalts of the Tibesti mountains, ($\epsilon\text{Nd} = 5$ to 7 ; Allegre et al., 1981). Some lake
470 mollusks analyzed in Wadi Behar Belema and Wadi Quoquin (two of these paleo-rivers) have
471 shown that the freshwater was significantly radiogenic ($\epsilon\text{Nd} = -2.2$ to -1.8) compared to the
472 Saharan dust (Osborne et al., 2008). Therefore, it has been suggested that these Libyan paleo-
473 rivers contributed an additional source of radiogenic Nd to the eastern Mediterranean Basin
474 during African Humid Periods (Scrivner et al., 2004). Seawater ϵNd records for core ODP site 971A
475 (proximal to the mouths of these paleo-rivers compared to more distal ODP Site 967C or core
476 LC21), were used to support this hypothesis during sapropel S5 (Osborne et al., 2008, 2010).
477 However, for different reasons, variations in the foraminiferal ϵNd obtained from cores located in
478 the eastern EMS cannot be entirely explained by changes in the Nd isotopic composition of the
479 water masses induced by lithogenic input from the African paleo-rivers. First, Sr and Nd isotopic
480 signatures of the detrital fraction of sediments close to the mouth of these Libyan paleo-rivers
481 (core CP10BC), have shown maximum sediment discharges during the sapropel S1b time interval
482 (Wu et al., 2016) whereas ϵNd records display more radiogenic values at the beginning of the AHP
483 (~ 14.8 cal kyr BP), reaching a maximum at ~ 13.5 cal kyr BP for core MD90-964 and at ~ 9.7 cal kyr
484 BP for core MS27PT (Fig. 5). Second, the sapropel time interval in cores MD90-964 and MS27PT, as
485 well as in several cores previously investigated throughout the EMS (Wu et al., 2019), is associated
486 with a continuous decrease in ϵNd values during the deposition of sapropel S1 indicating a more
487 radiogenic signature for the S1a than for the S1b time interval (Fig. 5). Finally, core CP10, which
488 should be susceptible to a significant influence from the discharge of Libyan paleo-river sediments
489 due to its proximal location does not in fact exhibit any influence on its seawater ϵNd record (Wu
490 et al., 2019). Therefore, while we cannot fully rule out a local influence of detrital discharge from
491 the Libyan paleo-rivers on seawater ϵNd , its contribution to Levantine deep-water masses can be
492 considered negligible.

493 In conclusion, the process of “boundary exchange” between water masses and volcanic sediment
494 along the margin of the eastern and northern Levantine Basin is one of the major sources of

495 lithogenic Nd to the Mediterranean Sea (Ayache et al., 2016), but neither changes in the inputs of
496 lithogenic Nd from the Nile River nor from the paleo-rivers of the North African margin can explain
497 the glacial-interglacial variability observed in the seawater ϵNd records of core MD90-964.

498 **5.2 Paleo-hydrological implications of the ϵNd records during glacial-interglacial** 499 **transitions and Terminations I and II**

500 The ϵNd records for the EMS display significant glacial and interglacial variations, ranging from
501 -2.0 ± 0.2 to -4.3 ± 0.2 , with more radiogenic values during glacial MIS6, 4, 3 and 2 (Fig. 4) that may
502 have been induced by the result of an increase in the residence time of deep-water masses in the
503 EMS and/or a decrease in the proportion of unradiogenic MAW flowing into the EMS.

504 Using a regional ocean-atmosphere coupled climate model, Vadsaria et al. (2019) have shown that
505 a reduction in the formation of deep water in the Eastern basin is associated with an increase in
506 deep-water ϵNd due to a longer interaction between the water masses and the radiogenic
507 sediments along the eastern margins of the EMS (Ayache et al., 2016). However, since the
508 ventilation of the EMDW was enhanced during glacial MIS2, 4 and 6, due to saltier and denser
509 surface water (Thunell and Williams, 1989; Béthoux et al., 1990; Myers et al., 1998a), the more
510 radiogenic ϵNd values for the EMDW during glacial periods cannot be attributed to a modification
511 of the residence time of deep-water masses. Moreover, several models have shown that exchange
512 between the Atlantic Ocean and the Mediterranean Sea may have been reduced by as much as
513 half during the glacial low sea-level stands, resulting in a higher longitudinal salinity gradient in the
514 Mediterranean Sea (Bryden et al., 1994; Myers et al., 1998b; Mikolajewicz, 2011; Grimm et al.,
515 2015). Periods of glacial low sea level may have caused a 50% reduction in water exchange
516 between the eastern and the western Mediterranean basins through the Sicilo-Tunisian Strait
517 (Mikolajewicz, 2011; Grimm et al., 2015). Consequently, taking into account that glacial periods
518 were associated with enhanced convection of deep water in the EMS, the more radiogenic ϵNd
519 observed for the glacial EMDW can be attributed to a decrease in the contribution of the Modified
520 Atlantic Water (MAW) to the eastern Mediterranean Basin. In this case, therefore, there is an
521 entrainment of radiogenic ϵNd surface water to the deep basin at the center of production of
522 deep-water masses. However, we cannot exclude that the decrease in zonal water exchange
523 between the WMS and the EMS during the glacial period favored also a longer contact time
524 between the EMDW and the radiogenic sediment draping the eastern Mediterranean continental

525 margin during this time. This hypothesis would need to be tested further using a regional
526 modeling approach.

527 However, we have tried to estimate the reduction of MAW to the EMS necessary to explain an
528 increase of 1.5 ϵ Nd unit observed in core MD90-964 during glacial time relative to the low values
529 of the MIS1 and 5 (out of sapropel and African Humid Periods) using a simple box-model for Nd in
530 the EMS established by Wu et al. (2019). We have used the present-day input of Nile river and
531 dust to the EMS (Nile \times 1, Dust \times 1; Fig.5 of Wu et al., 2019). Results suggest that the observed glacial
532 increase of ϵ Nd could be attributed to a decrease of MAW by 55 % relative to today. Such
533 variations are likely overestimated as the radiogenic Nd contribution from Nile could have also
534 been reduced during glacial period. Nevertheless, the calculated reduction of MAW inflow into the
535 EMS during glacial low sea-level stands agrees with the 50 % reduction in water exchange
536 between the eastern and the western Mediterranean basins through the Siculo-Tunisian Strait
537 quantified by Mikolajewicz, (2011) for the LGM.

538 The ϵ Nd record of core MD90-964 covers the last Terminations I and II. The significant decrease in
539 the ϵ Nd value (from -3.2 ± 0.2 to -4.4 ± 0.2) during Termination I begins at around 18 cal kyr BP and
540 is coeval with a similar decrease in $\delta^{13}\text{C}$ obtained from benthic foraminifera (Incarbona et al.,
541 2011; Sprovieri et al., 2012; Toucanne et al., 2012; Cornuault et al., 2016) (Fig. 6). The decrease of
542 the ϵ Nd during Termination II observed in core MD90-964 is also associated with a decrease of
543 benthic $\delta^{13}\text{C}$, which is particularly well marked in the Ionian Basin, close to the Siculo-Tunisian
544 Strait (Incarbona et al., 2011). The decrease in $\delta^{13}\text{C}$ obtained on benthic foraminifera has been
545 linked to a reduction in deep-water convection in the Mediterranean Sea, but the influence of an
546 increase in surface productivity cannot be excluded (Incarbona et al., 2011; Cornuault et al., 2016).
547 During both terminations, the decrease in ventilation suggested by the benthic foraminifera $\delta^{13}\text{C}$
548 record is not associated with more radiogenic values, as expected if the seawater residence time
549 in the EMS had increased. On the contrary, the ϵ Nd record shows a decrease suggesting a higher
550 contribution of unradiogenic AW to the Eastern Basin linked to the rise of the relative sea level
551 and enhanced water mass exchange between the eastern and western Mediterranean basins. The
552 timing of reduced ventilation and increase in Atlantic Water contribution to the eastern
553 Mediterranean basin is consistent with the ocean-biogeochemical model results obtained by
554 Grimm et al. (2015), which indicate that deep-water anoxia requires a long prelude of deep-water
555 stagnation of about 6 kyr, with no particularly strong eutrophication. The timing and duration of

556 the stagnation prelude agree with the mechanisms for ORL1 (organic-rich layer) deposition in the
557 western Mediterranean Sea proposed by Sierro et al. (2005).

558 In particular, the decreases in both benthic $\delta^{13}\text{C}$ and ϵNd before the sapropels S1 and S5 are
559 coeval with the end of Heinrich Stadial 1 and 11 (HS1 and HS11), respectively. It has been
560 postulated that an enhanced inflow of less salty seawater in the Mediterranean Sea during the
561 HS1 time interval favored a reduction in deep-water convection in the western basin and caused
562 the ORL1 deposition between 14.5 and 8.2 cal kyr BP (Cacho et al., 2002; Martínez-Ruiz et al.,
563 2003). However, this time interval is still associated with deep-water convection allowing the
564 transfer of unradiogenic ϵNd from MAW to the EMDW at the center of deep-water production in
565 the EMS. Our new ϵNd record from core MD90-964 suggests similar mechanisms during
566 Termination II, with a potential reduction in the salinity of the Atlantic Water flowing into the
567 Mediterranean Sea during the HS11 (Kandiano et al., 2014; Jiménez-Espejo et al., 2015; Grant et
568 al., 2016) and an increase in the proportion of MAW in the deep-water masses of the EMS, 5 to 6
569 kyr prior to the deposition of sapropel S5.

570 **5.3 Variability of the EMS during the African Humid Periods**

571 The ϵNd record of core MD90-964 reveals that African Humid Periods (maximum of summer
572 insolation) of the last climatic cycle are generally associated with more radiogenic ϵNd values of
573 the EMDW (Fig. 4). The sample from core MS27PT dated at ~ 9.7 cal kyr BP displays the most
574 radiogenic ϵNd value (-2.5 ± 0.2), which corresponds to the maximum of summer insolation
575 received by the Earth at 20°N (Figs. 4 and 6). The planktonic foraminifera $\delta^{18}\text{O}$ record from core
576 9509, located under the River Nile plume in the southeastern Levantine Basin (Fig. 1) (Almogi-
577 Labin et al., 2009), shows the most negative values (-1‰) at ~ 9.3 cal kyr BP, suggesting a large
578 input of freshwater from the Nile during this time. Such variations may therefore involve (i) a
579 more efficient exchange of Nd from seawater and river sediment plumes associated with an
580 intensification of the Nile River sediment discharge during the African Humid Periods (Revel et al.,
581 2010; Cornuault et al., 2016) and/or (ii) a longer residence time of water masses in the EMS during
582 time intervals of stratification of the water column that could have led to increased boundary-
583 exchange processes at the continental margin (Lacan and Jeandel, 2005).

584 Recent studies have shown that river sediment discharges can modify the Nd isotopic composition
585 of surrounding water masses (Singh et al., 2012; Chen et al., 2013; Goswami et al., 2014; Osborne
586 et al., 2014; Rousseau et al., 2015; Wu et al., 2015a), as recently observed in the Bay of Bengal for

587 a water depth greater than 2000 m (Yu et al., 2018). However, the ϵNd values of core BC07,
588 collected at a shallower water-depth (893 m) in the lower portion of the LIW, are less radiogenic
589 by 2 ϵNd units during the sapropel S1 time interval relative to the other ϵNd records available
590 nearby (core MD90-964). This suggests that lithogenic Nd from Nile river sediment plumes did not
591 play a major role in ϵNd variations of intermediate and deep-water masses in the eastern
592 Mediterranean Basin during the African Humid Period. However, Nile river sediment plumes could
593 partially explain the ϵNd variations during the deposition of sapropel S1 given that core MS27PT,
594 located closer to the Nile river mouth, is characterized by higher ϵNd amplitude compared to what
595 observed in core MD90-964.

596 Results from the recent regional circulation model developed by Vadsaria et al. (2019), using a
597 five-fold increase in Nile runoff during the deposition of sapropel S1, show more radiogenic ϵNd
598 values (by 2 ϵNd units) for the deep-water masses below 1200 m, associated with a sluggish
599 circulation, stagnation of deep water and consequent longer interaction with the surrounding
600 radiogenic margins. This result agrees well with ϵNd records obtained for sapropels S1 to S5 (cores
601 MS27PT and MD90-964) that display an increase of up to 2.5 ϵNd units (Figs. 5 and 6). In addition,
602 the less radiogenic values observed in core BC07 during sapropel S1 are also consistent with model
603 results for intermediate waters (near the LIW) (Vadsaria et al., 2019). Modeling outputs have
604 shown a modification of the sea surface circulation pattern favorable to the propagation of
605 unradiogenic western Mediterranean Sea waters into the intermediate waters of the Levantine
606 Basin. The resulting ϵNd decrease observed at intermediate water depth is related to less vigorous
607 circulation that also induces a reduction of the exchange with high-radiogenic material from the
608 east of the EMS. Consequently, distinct variations of ϵNd records for intermediate- and deep-
609 waters observed in cores BC07 and MD90-964 during the interval of sapropel S1 deposition are
610 supported by models and suggest deep-water stagnation and less vigorous circulation of the LIW.

611 The ϵNd record of core MS27PT shows an increase around 4 kyr before the deposition of sapropel
612 S1 (from 10.5 to 6.5 cal kyr BP, Bar-Matthews et al., 2000). This is in agreement with the recent
613 Nile sediment discharge records that indicate an increasing discharge at ~15 cal kyr BP that could
614 have induced a freshening of the Mediterranean Sea and a slow-down of the circulation (Revel et
615 al., 2010). Our new results allow us to investigate the potential for a time lag between seawater
616 ϵNd rise and sapropel onset for the previous sapropels S3, S4 and S5. The smectite/illite
617 mineralogical ratio of core MD90-964 (Fig. 4) enables estimating the Nile discharge over the last

618 climatic cycle (Zhao et al., 2011). This mineralogical ratio increases at about 15 cal kyr BP, in
619 agreement with an intensification of Nile river discharge prior to the deposition of sapropel S1
620 (Revel et al., 2010). Taking into consideration the relatively low time resolution of the record,
621 similar time lags can be observed between the seawater ϵNd record and the deposition of
622 sapropels S3 and S4 (Fig. 4). The seawater ϵNd values systematically increase before the intervals
623 of sapropels deposition but these shifts to more radiogenic values are not always associated with
624 variations in the smectite/illite ratio. The lower time resolution of the ϵNd record of core MD90-
625 964 around sapropel S5 does prevent us from clearly identifying a similar time lag.

626 The time interval coeval with sapropel S5 is characterized by lower ϵNd values relative to those of
627 sapropels S1 and S4, and to a lesser extent to those of sapropel S3. ODP Site 967C, which is at a
628 more distal position relative to the Nile River mouth, also displays comparable ϵNd values during
629 the S5 mid-point, with slightly less radiogenic values (of about 0.5 ϵNd units) at the limits of S5 (Fig.
630 6). African monsoon rainfall has been more intense during the time interval of the S5 deposition
631 than during sapropels S1 or S4 (Bar-Matthews et al., 2000), likely leading to more intense Nile
632 sediment and freshwater discharges. The lower $\delta^{18}\text{O}$ *G. ruber* values obtained from core MD90-
633 964 during S5 compared to S1 points to a more significant freshwater discharge from the Nile to
634 the studied site (Fig. 2C). This suggests that the higher contribution of unradiogenic MAW in this
635 period of particularly high relative sea level (Fig. 6A), may have overtaken the influence of an
636 increase in radiogenic Nd from the Nile input and/or of a lesser vigorous deep-water circulation in
637 the EMS during the deposition of sapropel S5. This would explain why the development of
638 sapropel S5 is not related to higher ϵNd values compared to other sapropels, such as S1 and S4.
639 For sapropel S4, the ϵNd record may indicate enhanced Nile river discharge, or more likely, a
640 reduction in EMS-WMS exchange induced by lower sea level during MIS5c compared to MIS5e (Fig.
641 6A). Further modeling studies are needed to estimate the relative contribution of the MAW to the
642 eastern Mediterranean Basin under the environmental conditions prevailing during the different
643 sapropel depositions and particularly during the high sea-level of S5.

644 **6. Conclusions**

645 Based on the foraminiferal ϵNd record of cores MD90-964 and MS27PT, located in the eastern
646 Levantine Basin, we provide evidence of significant glacial-interglacial variations in the inflow of
647 Atlantic Water to the EMS during the last climate cycle (last 145 kyr). We have demonstrated for
648 the first time that ϵNd values for the EMDW are systematically associated with more radiogenic

649 values during glacial Marine Isotope Stages. Such long-term glacial to interglacial variations in ϵNd
650 values cannot be solely the result of changes in Nile river discharge and Saharan dust inputs.
651 Decreases in ϵNd values during MIS5 and MIS1 interglacials have been attributed to an increase in
652 the contribution of unradiogenic MAW to the EMS related to high sea-level stands and enhanced
653 seawater exchange between the North Atlantic and the Mediterranean basins. Termination I and II
654 are associated with a decrease in seawater ϵNd in line with a decrease in the $\delta^{13}\text{C}$ obtained from
655 benthic foraminifera, suggesting a sluggish deep-sea ventilation in the EMS related to a higher
656 contribution of Atlantic Water in the EMS through the Siculo-Tunisian Strait during sea-level rise.

657 Superimposed on this long-term glacial-interglacial variation, a monsoon–precession induced
658 signal is distinguished in ϵNd records by more radiogenic values related to African Humid Periods
659 (and sapropel events). These periods of radiogenic ϵNd of the EMDW have been associated with
660 an intensification of Nile discharge and an increase in the residence time of deep-water masses in
661 the EMS, leading to an increase in the contact time between deep-water masses and radiogenic
662 sediments along the continental margin of the EMS.

663 Overall, our ϵNd records combined with previous ϵNd values obtained in the EMS reinforce the
664 hypothesis that a drastic reduction in the hydrological exchanges between the western and
665 eastern Mediterranean basins, and a subsequent higher proportion of Atlantic Water during sea
666 level rise may have preconditioned sapropel deposition in the EMS during the last climatic cycle,
667 as proposed by Grimm et al. (2015).

668

669 **Acknowledgements**

670 The research leading to this paper was funded by the French National Research Agency under the
671 "Investissements d'avenir" programme (Grant ANR-11-IDEX-0004-17-EURE-0006), the HAMOC
672 Project (Grant ANR-13-BS06-0003) and the INSU LEFE-IMAGO PALMEDS Project. We gratefully
673 acknowledge the support provided by Louise Bordier during Nd isotopic composition analyses. We
674 especially thank Adi Torfstein and an anonymous reviewer for their constructive reviews, which
675 significantly helped to improve this manuscript.

676

677

678 **Figure captions:**

679 Figure 1: (A) Bathymetric map of the Mediterranean Sea showing locations of core MD90-964
680 (33°02.75'N; 32°38.57'E; water depth 1375 m, length 32.12 m), core MS27PT (31°47.90'N,
681 29°27.70'E; water depth 1389 m, length 7.3 m) (blue dots) and all the other sites discussed in this
682 study (black dots) (Freydier et al., 2001; Scrivner et al., 2004; Osborne 2008, 2010; Cornuault et al.,
683 2018). The simplified modern Mediterranean water circulation is broadly indicated. Signatures of
684 Nd isotopic composition are displayed for the Nile River and aeolian dust (Grousset et Biscaye,
685 2005; Padoan et al., 2011; Scheuvens et al., 2013). The potential pathways of North-African paleo-
686 rivers are also depicted in light gray (Rohling et al., 2002; Wu et al., 2017). (B) Longitudinal
687 transect of annual mean salinity of the Mediterranean Sea (i.e. the red shading shown in (A); data
688 from WOA13). ϵ Nd values are represented by colored dots (Henry et al., 1994; Tachikawa et al.,
689 2004; Vance et al., 2004). The map and section were generated using Ocean Data View software
690 (Schlitzer, 2015).

691 Figure 2: Age models of cores MD90-964 and MS27PT: (A) age-depth curve for core MS27PT
692 (continuous line) interpolated from AMS ^{14}C dates (Revel et al., 2015; Bastian et al. 2017) and (B)
693 age-depth curve for core MD90-964 (dashed line) (Zhao et al., 2011). (C) $\delta^{18}\text{O}$ analyzed on
694 planktonic foraminifera *G. ruber* of core MD90-964 (continuous line) and MedStack composite
695 reference (dashed line; Lourens, 2004). (D) Organic carbon concentration of core MD90-964
696 sediment (Zhao et al., 2011). (E) $\delta^{18}\text{O}$ analyzed on *G. ruber* of core MS27PT. (F) Organic carbon
697 concentration of core MS27PT sediment. Black triangles correspond to the radiocarbon dates
698 obtained for core MS27PT. The Marine Isotope Stages (MIS) and time intervals of sapropel layers
699 are also reported.

700 Figure 3: (A) Nd isotopic composition (ϵ Nd) obtained from foraminifera of core MS27PT: ϵ Nd
701 values obtained from cleaning solution of *G. ruber* (solid green triangle), reductively cleaned *G.*
702 *ruber* (solid blue triangle), non-reductively cleaned *G. ruber* (solid red triangle), reductively
703 cleaned mixed planktonic foraminifera (solid blue rectangle), cleaning solution of mixed planktonic
704 foraminifera (solid green rectangle), non-reductively cleaned mixed planktonic foraminifera (solid
705 red rectangle); (B) ϵ Nd obtained on non-reductively cleaned mixed planktonic foraminifera (solid
706 black square) of core MD90-964 for the last 23 cal kyr BP. The Marine Isotope Stages (MIS) and
707 time intervals of sapropel S1 and AHP are also reported.

708 Figure 4: Variations in (A) the Relative Sea Level (RSL) (Grant et al., 2014) and (B) the summer
709 insolation (June and July) received by the Earth at 20°N, calculated using Analyseries software
710 (Paillard et al., 1996) for the last 160 kyr. (C) Variations of the $\delta^{18}\text{O}$ obtained from *G. ruber* of core
711 MD90-964 (Zhao et al., 2011); (D) Variations of the smectite/illite ratio of core MD90-964 (Zhao et
712 al. 2011); (E) Variations of the Nd isotopic composition (ϵNd) obtained from uncleaned mixed
713 planktonic foraminifera of core MD90-964 (this study); (F) Variations of the Total Organic Carbon
714 (wt%) of sediments from core MD90-964 (Zhao et al., 2011). The Marine Isotope Stages (MIS) and
715 time intervals of Sapropel S1 to S5 deposition are also reported.

716 Figure 5: Comparison between ϵNd records obtained in this study (cores MD90-964 and MS27PT)
717 and published records for the last 25 kyr. Core MD04-2722: Cornuault et al. (2018); cores BC07:
718 Freydier et al (2001); SL29: Wu et al. (2019); ODP Site 967C: Scrivner et al. (2004).

719 Figure 6: (A) Variations in Relative Sea Level (RSL) (Grant et al., 2014) and summer insolation (June
720 and July) received by the Earth at 20°N, calculated using Analyseries software (Paillard et al., 1996)
721 for last 160 kyr. (B) ϵNd record obtained from ODP Site 967C (Osborne et al., 2010); (C) ϵNd record
722 obtained from non-reductively cleaned mixed planktonic foraminifera of core MD90-964 (this
723 study); (D) ϵNd record obtained from non-reductively cleaned mixed planktonic foraminifera of
724 core MS27PT (this study); (E) compilation of $\delta^{13}\text{C}$ obtained from benthic foraminifera from
725 Mediterranean cores. Records of $\delta^{13}\text{C}$ obtained from benthic foraminifera are published as
726 followed: MD04-2722 by Cornuault et al. (2016); MD01-2472 by Toucanne et al. (2012); ODP Site
727 963 by Incarbona et al. (2011); MD95-2043 by Cacho et al. (2007).

728

729 **Table captions:**

730 Table 1: Results of Nd isotopic composition obtained from planktonic foraminifera samples from
731 core MS27PT. Nd isotopic composition were obtained from reductively cleaned foraminifera,
732 cleaning solution, or uncleaned foraminifera. Foraminifera are monospecific (*G. ruber*) or
733 multispecific (mixed planktonic foraminifera). The age of sediments have been determined by
734 linear interpolation between 22 AMS ^{14}C dates of foraminifera (Revel et al., 2010, 2015; Bastian et
735 al., 2017; Menot et al., 2020).

736 Table 2: Results of Nd isotopic composition obtained from planktonic foraminifera samples from
737 core MD90-964. The age of sediments have been obtained by the correlation between the *G.*

738 *ruber* $\delta^{18}\text{O}$ record and the Mediterranean *G. ruber* stack compiled by Lourens (2004) (Zhao et al.,
739 2011).

740

741 References

- 742 Allegre, C.J., Dupré, B., Lambert, B., Richard, P., 1981. The subcontinental versus suboceanic
743 debate. Lead-neodymium-strontium isotopes in primary alkali basalts from a shield area, the
744 Ahaggar volcanic suite. *Earth Planet Sci Lett* 52, 85–92
- 745 Allen, J.R.M., Huntley, B., Brandt, U., Brauer, A., Hubberten, H., Keller, J., Kraml, M., Mackensen, A.,
746 Mingram, J., Negendank, J.F.W., Nowaczyk, N.R., Oberhänsli, H., Watts, W.A., Wulf, S.,
747 Zolitschka, B., 1999. Rapid environmental changes in southern Europe during the last glacial
748 period. *Nature* 400, 740–743. <https://doi.org/10.1038/23432>
- 749 Almogi-Labin, A., Bar-Matthews, M., Shriki, D., Kolosovsky, E., Paterne, M., Schilman, B., Ayalon, A.,
750 Aizenshtat, Z., Matthews, A., 2009. Climatic variability during the last ~90 ka of the southern
751 and northern Levantine Basin as evident from marine records and speleothems. *Quat. Sci. Rev.*
752 28, 2882–2896. <https://doi.org/10.1016/j.quascirev.2009.07.017>
- 753 Angue Minto’o, C.M., Bassetti, M.A., Morigi, C., Ducassou, E., Toucanne, S., Jouet, G., Mulder, T.,
754 2015. Levantine intermediate water hydrodynamic and bottom water ventilation in the
755 northern Tyrrhenian Sea over the past 56,000 years: New insights from benthic foraminifera
756 and ostracods. *Quat. Int.* 357, 295–313. <https://doi.org/10.1016/j.quaint.2014.11.038>
- 757 Arbuszewski, J.A., Demenocal, P.B., Cléroux, C., Bradtmiller, L., Mix, A., 2013. Meridional shifts of
758 the Atlantic intertropical convergence zone since the Last Glacial Maximum. *Nat. Geosci.* 6,
759 959–962. <https://doi.org/10.1038/ngeo1961>
- 760 Ayache, M., Dutay, J.-C., Arsouze, T., Révillon, S., Beuvier, J., Jeandel, C., 2016. High resolution
761 neodymium characterization along the Mediterranean margins and modeling of ϵNd
762 distribution in the Mediterranean basins. *Biogeosciences Discuss.* 1–31.
763 <https://doi.org/10.5194/bg-2016-109>
- 764 Bar-Matthews, M., Ayalon, A., Kaufman, A., 2000. Timing and hydrological conditions of Sapropel
765 events in the Eastern Mediterranean, as evident from speleothems, Soreq cave, Israel. *Chem.*
766 *Geol.* 169, 145–156. [https://doi.org/10.1016/S0009-2541\(99\)00232-6](https://doi.org/10.1016/S0009-2541(99)00232-6)
- 767 Bar-Matthews, M., Ayalon, A., Vaks, A., Frumkin, A., 2017. Climate and Environment
768 Reconstructions Based on Speleothems from the Levant. In Y. Enzel & O. Bar-Yosef (Eds.),
769 *Quaternary of the Levant: Environments, Climate Change, and Humans* (pp. 151-164).
770 Cambridge: Cambridge University Press. doi:10.1017/9781316106754.017
- 771 Barrows, T.T., Williams, M.A.J., Mills, S.C., Duller, G.A.T., Fifield, L.K., Haberlah, D., Tims, S.G.,
772 Williams, F.M., 2014. A White Nile megalake during the last interglacial period. *Geology* 42,
773 163–166. <https://doi.org/10.1130/G35238.1>
- 774 Bartov, Y., Goldstein, S.L., Stein, M., Enzel, Y., 2003. Catastrophic arid episodes in the Eastern
775 Mediterranean linked with the North Atlantic Heinrich events. *Geology* 31, 439.
776 [https://doi.org/10.1130/0091-7613\(2003\)031<0439:CAEITE>2.0.CO;2](https://doi.org/10.1130/0091-7613(2003)031<0439:CAEITE>2.0.CO;2)
- 777 Bastian, L., Revel, M., Bayon, G., Dufour, A., Vigier, N., 2017. Abrupt response of chemical
778 weathering to Late Quaternary hydroclimate changes in northeast Africa. *Sci. Rep.* 7.
779 <https://doi.org/10.1038/srep44231>
- 780 Béthoux, J.P., Gentili, B., Raunet, J., Tailliez, D., 1990. Warming trend in the Western
781 Mediterranean Deep Water. *Nature* 347, 660–662
- 782 Bianchi, D., Zavatarelli, M., Pinardi, N., Capozzi, R., Capotondi, L., Corselli, C., Masina, S., 2006.

783 Simulations of ecosystem response during the sapropel S1 deposition event.
784 *Palaeogeography Palaeoclimatology Palaeoecology* 235, 265–287

785 Blanchet, C.L., Contoux, C., Leduc, G., 2015. Runoff and precipitation dynamics in the Blue and
786 White Nile catchments during the mid-Holocene: A data-model comparison. *Quat. Sci. Rev.*
787 130, 222–230. <https://doi.org/10.1016/J.QUASCIREV.2015.07.014>

788 Blanchet, C.L., Tjallingii, R., Frank, M., Lorenzen, J., Reitz, A., Brown, K., Feseker, T., Brückmann, W.,
789 2013. High- and low-latitude forcing of the Nile River regime during the Holocene inferred
790 from laminated sediments of the Nile deep-sea fan. *Earth Planet. Sci. Lett.* 364, 98–110.
791 <https://doi.org/10.1016/J.EPSL.2013.01.009>

792 Bryden, H.L., Candela, J., Kinder, T.H., 1994. Exchange through the Strait of Gibraltar. *Prog.*
793 *Oceanogr.* 33, 201–248. [https://doi.org/10.1016/0079-6611\(94\)90028-0](https://doi.org/10.1016/0079-6611(94)90028-0)

794 Cacho, I., Grimalt, J.O., Canals, M., 2002. Response of the Western Mediterranean Sea to rapid
795 climatic variability during the last 50,000 years: a molecular biomarker approach. *J. Mar. Syst.*
796 33–34, 253–272. [https://doi.org/10.1016/S0924-7963\(02\)00061-1](https://doi.org/10.1016/S0924-7963(02)00061-1)

797 Castañeda, I.S., Schouten, S., Pätzold, J., Lucassen, F., Kasemann, S., Kuhlmann, H., Schefuß, E.,
798 2016. Hydroclimate variability in the Nile River Basin during the past 28,000 years. *Earth*
799 *Planet. Sci. Lett.* 438, 47–56. <https://doi.org/10.1016/j.epsl.2015.12.014>

800 Chen, T.-Y., Stumpf, R., Frank, M., Bełdowski, J., Staubwasser, M., 2013. Contrasting geochemical
801 cycling of hafnium and neodymium in the central Baltic Sea. *Geochim. Cosmochim. Acta* 123,
802 166–180. <https://doi.org/10.1016/J.GCA.2013.09.011>

803 Copard, K., Colin, C., Douville, E., Freiwald, A., Gudmundsson, G., de Mol, B., Frank, N., 2010. Nd
804 isotopes in deep-sea corals in the North-eastern Atlantic. *Quat. Sci. Rev.* 29, 2499–2508

805 Cornuault, M., Tachikawa, K., Vidal, L., Guihou, A., Siani, G., Deschamps, P., Bassinot, F., Revel, M.,
806 2018. Circulation Changes in the Eastern Mediterranean Sea Over the Past 23,000 Years
807 Inferred From Authigenic Nd Isotopic Ratios. *Paleoceanogr. Palaeoclimatology.*
808 <https://doi.org/10.1002/2017PA003227>

809 Cornuault, M., Vidal, L., Tachikawa, K., Licari, L., Rouaud, G., Sonzogni, C., Revel, M., 2016. Deep
810 water circulation within the eastern Mediterranean Sea over the last 95 kyr: New insights
811 from stable isotopes and benthic foraminiferal assemblages. *Palaeogeogr. Palaeoclimatol.*
812 *Palaeoecol.* 459, 1–14. <https://doi.org/10.1016/J.PALAEO.2016.06.038>

813 Cramp, A., O’Sullivan, G., 1999. Neogene sapropels in the Mediterranean: A review. *Mar. Geol.*
814 153, 11–28. [https://doi.org/10.1016/S0025-3227\(98\)00092-9](https://doi.org/10.1016/S0025-3227(98)00092-9)

815 De Lange, G.J., Thomson, J., Reitz, A., Slomp, C.P., Principato, M.S., Erba, E., Corselli, C., 2008.
816 Synchronous basin-wide formation and redox-controlled preservation of a Mediterranean
817 sapropel. *Nature Geoscience* 1, 606–610

818 DeMenocal, P., Ortiz, J., Guilderson, T., Sarnthein, M., 2000. Coherent High- and Low-Latitude
819 Climate Variability During the Holocene Warm Period. *Science* (80-.). 288, 2198–2202.
820 <https://doi.org/10.1126/science.288.5474.2198>

821 Dubois-Dauphin, Q., Montagna, P., Siani, G., Douville, E., Wienberg, C., Hebbeln, D., Liu, Z., Kallel,
822 N., Dapoigny, A., Revel, M., Pons-Branchu, E., Taviani, M., Colin, C., 2017. Hydrological
823 variations of the intermediate water masses of the western Mediterranean Sea during the
824 past 20 ka inferred from neodymium isotopic composition in foraminifera and cold-water
825 corals. *Clim. Past* 13, 17–37. <https://doi.org/10.5194/cp-13-17-2017>

826 Ehrmann, W., Schmiedl, G., Beuscher, S., Krüger, S., 2017. Intensity of African Humid Periods
827 Estimated from Saharan Dust Fluxes. *PLoS One* 12, e0170989.
828 <https://doi.org/10.1371/journal.pone.0170989>

829 Ehrmann, W., Schmiedl, G., Seidel, M., Krüger, S., Schulz, H., 2016. A distal 140 kyr sediment
830 record of Nile discharge and East African monsoon variability. *Clim. Past* 12, 713–727.

831 <https://doi.org/10.5194/cp-12-713-2016>

832 Ehrmann, W., Seidel, M., Schmiedl, G., 2013. Dynamics of Late Quaternary North African humid
833 periods documented in the clay mineral record of central Aegean Sea sediments. *Glob. Planet.*
834 *Change* 107, 186–195. <https://doi.org/10.1016/J.GLOPLACHA.2013.05.010>

835 Emeis, K.-C., Schulz, H., Struck, U., Rossignol-Strick, M., Erlenkeuser, H., Howell, M.W., Kroon, D.,
836 Mackensen, A., Ishizuka, S., Oba, T., Sakamoto, T., Koizumi, I., 2003. Eastern Mediterranean
837 surface water temperatures and $\delta^{18}\text{O}$ composition during deposition of sapropels in the late
838 Quaternary. *Paleoceanography* 18, n/a-n/a. <https://doi.org/10.1029/2000PA000617>

839 Filippidi, A., Triantaphyllou, M.V., De Lange, G.J., 2016. Eastern-Mediterranean ventilation
840 variability during sapropel S1 formation, evaluated at two sites influenced by deep-water
841 formation from Adriatic and Aegean Seas. *Quaternary Science Reviews* 144, 95–106

842 Fontugne, M., Arnold, M., Labeyrie, L., Paterne, M., Calvert, S.E., Duplessy, J.C., 1994.
843 Paleoenvironment, sapropel chronology and Nile river discharge during the last 20,000 years
844 as indicated by deep-sea sediment records in the eastern Mediterranean. *Radiocarbon* 34,
845 75–88.

846 Foucault, A., Stanley, D.J., 1989. Late Quaternary palaeoclimatic oscillations in East Africa recorded
847 by heavy minerals in the Nile delta. *Nature* 339, 44–46. <https://doi.org/10.1038/339044a0>

848 Freydier, R., Michard, A., De Lange, G., Thomson, J., 2001. Nd isotopic compositions of Eastern
849 Mediterranean sediments: tracers of the Nile influence during sapropel S1 formation? *Mar.*
850 *Geol.* 177, 45–62. [https://doi.org/10.1016/S0025-3227\(01\)00123-2](https://doi.org/10.1016/S0025-3227(01)00123-2)

851 Frigola, J., Moreno, A., Cacho, I., Canals, M., Sierro, F.J., Flores, J.A., Grimalt, J.O., 2008. Evidence of
852 abrupt changes in Western Mediterranean Deep Water circulation during the last 50kyr: A
853 high-resolution marine record from the Balearic Sea. *Quat. Int.* 181, 88–104.
854 <https://doi.org/10.1016/j.quaint.2007.06.016>

855 Garzanti, E., Andò, S., Padoan, M., Vezzoli, G., El Kammar, A., 2015. The modern Nile sediment
856 system: Processes and products. *Quat. Sci. Rev.* 130, 9–56.
857 <https://doi.org/10.1016/J.QUASCIREV.2015.07.011>

858 Gasse, F., 2000. Hydrological changes in the African tropics since the Last Glacial Maximum, in:
859 *Quaternary Science Reviews*. pp. 189–211. [https://doi.org/10.1016/S0277-3791\(99\)00061-X](https://doi.org/10.1016/S0277-3791(99)00061-X)

860 Goswami, V., Singh, S.K., Bhushan, R., 2014. Impact of water mass mixing and dust deposition on
861 Nd concentration and ϵNd of the Arabian Sea water column. *Geochim. Cosmochim. Acta* 145,
862 30–49. <https://doi.org/10.1016/J.GCA.2014.09.006>

863 Grant, K.M., Rohling, E.J., Bronk Ramsey, C., Cheng, H., Edwards, R.L., Florindo, F., Heslop, D.,
864 Marra, F., Roberts, A.P., Tamisiea, M.E., Williams, F., 2014. Sea-level variability over five
865 glacial cycles. *Nat. Commun.* 5, 5076

866 Grant, K.M., Grimm, R., Mikolajewicz, U., Marino, G., Ziegler, M., Rohling, E.J., 2016. The timing of
867 Mediterranean sapropel deposition relative to insolation, sea-level and African monsoon
868 changes. *Quat. Sci. Rev.* 140, 125–141. <https://doi.org/10.1016/J.QUASCIREV.2016.03.026>

869 Grimm, R., Maier-Reimer, E., Mikolajewicz, U., Schmiedl, G., Müller-Navarra, K., Adloff, F., Grant,
870 K.M., Ziegler, M., Lourens, L.J., Emeis, K.C., 2015. Late glacial initiation of Holocene eastern
871 Mediterranean sapropel formation. *Nat. Commun.* 6, 7099.
872 <https://doi.org/10.1038/ncomms8099>

873 Henry, F., Jeandel, C., Dupré, B., Minster, J.-F., 1994. Particulate and dissolved Nd in the western
874 Mediterranean Sea: Sources, fate and budget. *Mar. Chem.* 45, 283–305.
875 [https://doi.org/10.1016/0304-4203\(94\)90075-2](https://doi.org/10.1016/0304-4203(94)90075-2)

876 Incarbona, A., Sprovieri, M., Lirer, F., Sprovieri, R., 2011. Surface and deep water conditions in the
877 Sicily channel (central Mediterranean) at the time of sapropel S5 deposition. *Palaeogeogr.*
878 *Palaeoclimatol. Palaeoecol.* 306, 243–248. <https://doi.org/10.1016/J.PALAEO.2011.04.030>

- 879 Jacobsen, S.B., Wasserburg, G.J., 1980. Sm-Nd isotopic evolution of chondrites. *Earth Planet. Sci.*
880 *Lett.* 50, 139–155. [https://doi.org/10.1016/0012-821X\(80\)90125-9](https://doi.org/10.1016/0012-821X(80)90125-9)
- 881 Jilbert, T., Reichert, G.J., Aeschlimann, B., Gunther, D., Boer, W., de Lange, G.J., 2010.
882 Climatecontrolled multidecadal variability in North African dust transport to the
883 Mediterranean. *Geology* 38, 19–22
- 884 Jiménez-Espejo, F.J., Pardos-Gené, M., Martínez-Ruiz, F., García-Alix, A., van de Flierdt, T.,
885 Toyofuku, T., Bahr, A., Kreissig, K., 2015. Geochemical evidence for intermediate water
886 circulation in the westernmost Mediterranean over the last 20kyrBP and its impact on the
887 Mediterranean Outflow. *Glob. Planet. Change* 135, 38–46.
888 <https://doi.org/10.1016/j.gloplacha.2015.10.001>
- 889 Kallel, N., Paterne, M., Labeyrie, L., Duplessy, J.-C., Arnold, M., 1997. Temperature and salinity
890 records of the Tyrrhenian Sea during the last 18,000 years. *Palaeogeogr. Palaeoclimatol.*
891 *Palaeoecol.* 135, 97–108. [https://doi.org/10.1016/S0031-0182\(97\)00021-7](https://doi.org/10.1016/S0031-0182(97)00021-7)
- 892 Kandiano, E.S., Bauch, H.A., Fahl, K., 2014. Last interglacial surface water structure in the western
893 Mediterranean (Balearic) Sea: Climatic variability and link between low and high latitudes.
894 *Glob. Planet. Change* 123, 67–76. <https://doi.org/10.1016/J.GLOPLACHA.2014.10.004>
- 895 Krom, M., Cliff, R., Eijsink, L., Herut, B., Chester, R., 1999. The characterisation of Saharan dusts
896 and Nile particulate matter in surface sediments from the Levantine basin using Sr isotopes.
897 *Mar. Geol.* 155, 319–330. [https://doi.org/10.1016/S0025-3227\(98\)00130-3](https://doi.org/10.1016/S0025-3227(98)00130-3)
- 898 Krom, M.D., Stanley, J.D., Cliff, R.A., Woodward, J.C., 2002. Nile River sediment fluctuations over
899 the past 7000 yr and their key role in sapropel development. *Geology* 30, 71.
900 [https://doi.org/10.1130/0091-7613\(2002\)030<0071:NRSFOT>2.0.CO;2](https://doi.org/10.1130/0091-7613(2002)030<0071:NRSFOT>2.0.CO;2)
- 901 Lacan, F., Jeandel, C., 2005. Neodymium isotopes as a new tool for quantifying exchange fluxes at
902 the continent–ocean interface. *Earth Planet. Sci. Lett.* 232, 245–257.
903 <https://doi.org/10.1016/j.epsl.2005.01.004>
- 904 Lamb, H.F., Bates, C.R., Bryant, C.L., Davies, S.J., Huws, D.G., Marshall, M.H., Roberts, H.M., 2018.
905 150,000-year palaeoclimate record from northern Ethiopia supports early, multiple dispersals
906 of modern humans from Africa. *Sci. Rep.* 8, 1077. <https://doi.org/10.1038/s41598-018-19601-w>
- 908 Langgut, D., Almogi-Labin, A., Bar-Matthews, M., Weinstein-Evron, M., 2011. Vegetation and
909 climate changes in the South Eastern Mediterranean during the Last Glacial-Interglacial cycle
910 (86 ka): new marine pollen record. *Quat. Sci. Rev.* 30, 3960–3972.
911 <https://doi.org/10.1016/J.QUASCIREV.2011.10.016>
- 912 Larrasoana, J.C., Roberts, A.P., Rohling, E.J., Winkelhofer, M., Wehausen, R., 2003. Three million
913 years of monsoon variability over the northern Sahara. *Clim. Dyn.* 21, 689–698.
914 <https://doi.org/10.1007/s00382-003-0355-z>
- 915 Lascaratos, A., Williams, R.G., Tragou, E., 1993. A mixed-layer study of the formation of Levantine
916 intermediate water. *J. Geophys. Res.* 98, 14739. <https://doi.org/10.1029/93JC00912>
- 917 Lourens, L.J., 2004. Revised tuning of Ocean Drilling Program Site 964 and KC01B (Mediterranean)
918 and implications for the $\delta^{18}O$, teph.pdf.
- 919 Lugmair, G.W., Shimamura, T., Lewis, R.S., Anders, E., 1983. Samarium-146 in the Early Solar
920 System: Evidence from Neodymium in the Allende Meteorite. *Science* (80-). 222, 1015–1018.
921 <https://doi.org/10.1126/science.222.4627.1015>
- 922 Malanotte-Rizzoli, P., Manca, B.B., D'Alcala, M.R., Theocharis, A., Brenner, S., Budillon, G., Ozsoy,
923 E., 1999. The Eastern Mediterranean in the 80s and in the 90s: the big transition in the
924 intermediate and deep circulations. *Dyn. Atmos. Ocean.* 29, 365–395.
925 [https://doi.org/10.1016/S0377-0265\(99\)00011-1](https://doi.org/10.1016/S0377-0265(99)00011-1)
- 926 Martínez-Ruiz, F., Paytan, A., Kastner, M., González-Donoso, J.M., Linares, D., Bernasconi, S.M.,

927 Jimenez-Espejo, F.J., 2003. A comparative study of the geochemical and mineralogical
928 characteristics of the S1 sapropel in the western and eastern Mediterranean. *Palaeogeogr.*
929 *Palaeoclimatol. Palaeoecol.* 190, 23–37. [https://doi.org/10.1016/S0031-0182\(02\)00597-7](https://doi.org/10.1016/S0031-0182(02)00597-7)

930 Martrat, B., Grimalt, J.O., Lopez-Martinez, C., Cacho, I., Sierro, F.J., Flores, J.A., Zahn, R., Canals, M.,
931 Curtis, J.H., Hodell, D.A., 2004. Abrupt temperature changes in the Western Mediterranean
932 over the past 250,000 years. *Science* (80-). 306, 1762–1765.
933 <https://doi.org/10.1126/science.1101706>

934 Melki, T., Kallel, N., Jorissen, F.J., Guichard, F., Dennielou, B., Berné, S., Labeyrie, L., Fontugne, M.,
935 2009. Abrupt climate change, sea surface salinity and paleoproductivity in the western
936 Mediterranean Sea (Gulf of Lion) during the last 28 kyr. *Palaeogeogr. Palaeoclimatol.*
937 *Palaeoecol.* 279, 96–113. <https://doi.org/10.1016/j.palaeo.2009.05.005>

938 Ménot, G., Pivot, S., Bouloubassi, I., Davtian, N., Hennekam, R., Bosch, D, Ducassou, E., Bard, E.,
939 Migeon, S., Revel, M., 2020. Timing and stepwise transitions of the African Humid Period
940 from geochemical proxies in the Nile deep-sea fan sediments. *Quaternary Science Reviews*
941 228.

942 Mercone, D., Thomson, J., Croudace, I.W., Siani, G., Paterne, M., Troelstra, S., Croudace, L.W., Siani,
943 G., Paterne, M., Troelstra, S., 2000. Duration of S1, the most recent sapropel in the eastern
944 Mediterranean Sea, as indicated by accelerator mass spectrometry radiocarbon and
945 geochemical evidence. *Paleoceanography* 15, 336–347.
946 <https://doi.org/10.1029/1999PA000397>

947 Mikolajewicz, U., 2011. Climate of the Past Modeling Mediterranean Ocean climate of the Last
948 Glacial Maximum 7, 161–180. <https://doi.org/10.5194/cp-7-161-2011>

949 Millot, C., 1999. Circulation in the Western Mediterranean Sea. *J. Mar. Syst.* 20, 423–442.
950 [https://doi.org/10.1016/S0924-7963\(98\)00078-5](https://doi.org/10.1016/S0924-7963(98)00078-5)

951 Millot, C., Candela, J., Fuda, J.-L., Tber, Y., 2006. Large warming and salinification of the
952 Mediterranean outflow due to changes in its composition. *Deep Sea Res. Part I Oceanogr. Res.*
953 *Pap.* 53, 656–666. <https://doi.org/10.1016/j.dsr.2005.12.017>

954 Molina-Kescher, M., Frank, M., Hathorne, E.C., 2014. Nd and Sr isotope compositions of different
955 phases of surface sediments in the South Pacific: Extraction of seawater signatures, boundary
956 exchange, and detrital/dust provenance. *Geochemistry, Geophys. Geosystems* 15, 3502–3520.
957 <https://doi.org/10.1002/2014GC005443>

958 Murat, A., Got, H., 2000. Organic carbon variations of the eastern Mediterranean Holocene
959 sapropel: a key for understanding formation processes. *Palaeogeography, Palaeoclimatology,*
960 *Palaeoecology* 158, 241-257. Myers, P.G., Haines, K., Rohling, E.J., 1998a. Modeling the
961 paleocirculation of the Mediterranean: The Last Glacial Maximum and the Holocene with
962 emphasis on the formation of sapropel S1. *Paleoceanography* 13, 586–606.
963 <https://doi.org/10.1029/98PA02736>

964 Myers, P.G., Haines, K., Rohling, E.J., 1998b. Myers, Haines, Rohling - 1998 - Modeling the
965 paleocirculation of the Mediterranean The Last Glacial Maximum and the Holocene with
966 *emphas.pdf*.

967 Myers, P.G., 2002. Flux-forced simulations of the paleocirculation of the Mediterranean.
968 *Paleoceanography* 17, 1009. Doi:10.1029/2000PA000613.

969 Osborne, A.H., Haley, B.A., Hathorne, E.C., Flögel, S., Frank, M., 2014. Neodymium isotopes and
970 concentrations in Caribbean seawater: Tracing water mass mixing and continental input in a
971 semi-enclosed ocean basin. *Earth Planet. Sci. Lett.* 406, 174–186.
972 <https://doi.org/10.1016/j.epsl.2014.09.011>

973 Osborne, A.H., Marino, G., Vance, D., Rohling, E.J., 2010. Eastern Mediterranean surface water Nd
974 during Eemian sapropel S5: monitoring northerly (mid-latitude) versus southerly (sub-

975 tropical) freshwater contributions. *Quat. Sci. Rev.* 29, 2473–2483.

976 Osborne, A.H., Vance, D., Rohling, E.J., Barton, N., Rogerson, M., Fello, N., 2008. A humid corridor
977 across the Sahara for the migration of early modern humans out of Africa 120,000 years ago.
978 *Proc. Natl. Acad. Sci.* 105, 16444–16447.

979 Padoan, M., Garzanti, E., Harlavan, Y., Villa, I.M., 2011. Tracing Nile sediment sources by Sr and Nd
980 isotope signatures (Uganda, Ethiopia, Sudan). *Geochim. Cosmochim. Acta* 75, 3627–3644.
981 <https://doi.org/10.1016/J.GCA.2011.03.042>.

982 Paillard, D., Labeyrie, L., Yiou P., 1996. Analyseries 1.0: A Macintosh software for the analysis of
983 geographical timeseries. *Eos Trans. AGU*, 77, 379.

984 Pinardi, N., Masetti, E., 2000. Variability of the large scale general circulation of the Mediterranean
985 Sea from observations and modelling: a review. *Palaeogeography Palaeoclimatology*
986 *Palaeoecology* 158, 153–174.

987 Piotrowski, A.M., Galy, A., Nicholl, J.A.L., Roberts, N., Wilson, D.J., Clegg, J.A., Yu, J., 2012.
988 Reconstructing deglacial North and South Atlantic deep water sourcing using foraminiferal Nd
989 isotopes. *Earth Planet. Sci. Lett.* 357–358, 289–297.
990 <https://doi.org/10.1016/J.EPSL.2012.09.036>

991 Revel, M., Colin, C., Bernasconi, S., Combourieu-Nebout, N., Ducassou, E., Grousset, F.E., Rolland,
992 Y., Migeon, S., Bosch, D., Brunet, P., Zhao, Y., Mascle, J., 2014. 21,000 Years of Ethiopian
993 African monsoon variability recorded in sediments of the western Nile deep-sea fan. *Reg.*
994 *Environ. Chang.* 14, 1685–1696. <https://doi.org/10.1007/s10113-014-0588-x>

995 Revel, M., Ducassou, E., Grousset, F.E.E., Bernasconi, S.M.M., Migeon, S., Revillon, S., Mascle, J.,
996 Murat, A., Zaragosi, S., Bosch, D., 2010. 100,000 Years of African monsoon variability
997 recorded in sediments of the Nile margin. *Quat. Sci. Rev.* 29, 1342–1362.
998 <https://doi.org/10.1016/j.quascirev.2010.02.006>

999 Revel, M., Ducassou, E., Skonieczny, C., Colin, C., Bastian, L., Bosch, D., Migeon, S., Mascle, J., 2015.
1000 20,000 years of Nile River dynamics and environmental changes in the Nile catchment area as
1001 inferred from Nile upper continental slope sediments. *Quat. Sci. Rev.* 130, 200–221.
1002 <https://doi.org/10.1016/J.QUASCIREV.2015.10.030>

1003 Roberts, N.L., Piotrowski, A.M., Elderfield, H., Eglinton, T.I., Lomas, M.W., 2012. Rare earth
1004 element association with foraminifera. *Geochim. Cosmochim. Acta* 94, 57–71.
1005 <https://doi.org/10.1016/j.gca.2012.07.009>

1006 Robinson, A.R., Leslie, W.G., Theocharis, A., Lascaratos, A., 2001. Mediterranean sea circulation.
1007 *Ocean Curr.* 1, 19.

1008 Roether, W., Manca, B.B., Klein, B., Bregant, D., Georgopoulos, D., Beitzel, V., Kovacevic, V.,
1009 Luchetta, A., 1996. Recent changes in eastern Mediterranean deep waters. *Science* 271, 333–
1010 335

1011 Rohling, E.J., 1994. Review and new aspects concerning the formation of eastern Mediterranean
1012 sapropels. *Mar. Geol.* 122, 1–28. [https://doi.org/10.1016/0025-3227\(94\)90202-X](https://doi.org/10.1016/0025-3227(94)90202-X)

1013 Rohling, E.J., Cane, T.R., Bouloubassi, I., Kemp, A.E.S., Kroon, D., Schiebel, R., Lorre, A., Emeis, K.C.,
1014 Cooke, S., Jorissen, F.J., Sprovieri, M., 2002. African monsoon variability during the previous
1015 interglacial maximum, *Earth and Planetary Science Letters*. [https://doi.org/10.1016/S0012-](https://doi.org/10.1016/S0012-821X(02)00775-6)
1016 [821X\(02\)00775-6](https://doi.org/10.1016/S0012-821X(02)00775-6)

1017 Rohling, E.J., Den Dulk, M., Pujol, C., Vergnaud-Grazzini, C., 1995. Abrupt hydrographic change in
1018 the Alboran Sea (western Mediterranean) around 8000 yrs BP. *Deep Sea Res. Part I Oceanogr.*
1019 *Res. Pap.* 42, 1609–1619. [https://doi.org/10.1016/0967-0637\(95\)00069-I](https://doi.org/10.1016/0967-0637(95)00069-I)

1020 Rohling, E.J., Marino, G., Grant, K.M., 2015. Mediterranean climate and oceanography, and the
1021 periodic development of anoxic events (sapropels). *Earth-Science Rev.* 143, 62–97.
1022 <https://doi.org/10.1016/j.earscirev.2015.01.008>

- 1023 Rossignol-Strick, M., Nesteroff, W., Olive, P., Vergnaud-Grazzini, C., 1982. After the deluge:
 1024 Mediterranean stagnation and sapropel formation. *Nature* 285, 105–110.
 1025 <https://doi.org/10.1038/295105a0>
- 1026 Rousseau, T.C.C., Sonke, J.E., Chmeleff, J., van Beek, P., Souhaut, M., Boaventura, G., Seyler, P.,
 1027 Jeandel, C., 2015. Rapid neodymium release to marine waters from lithogenic sediments in
 1028 the Amazon estuary. *Nat. Commun.* 6, 7592. <https://doi.org/10.1038/ncomms8592>
- 1029 Scheuvens, D., Schütz, L., Kandler, K., Ebert, M., Weinbruch, S., 2013. Bulk composition of northern
 1030 African dust and its source sediments — A compilation. *Earth-Science Rev.* 116, 170–194.
 1031 <https://doi.org/10.1016/j.earscirev.2012.08.005>
- 1032 Schmiidl, G., Kuhnt, T., Ehrmann, W., Emeis, K.-C.C., Hamann, Y., Kotthoff, U., Dulski, P., Pross, J.,
 1033 2010. Climatic forcing of eastern Mediterranean deep-water formation and benthic
 1034 ecosystems during the past 22 000 years. *Quat. Sci. Rev.* 29, 3006–3020.
 1035 <https://doi.org/10.1016/j.quascirev.2010.07.002>
- 1036 Schmiidl, G., Mitschele, A., Beck, S., Emeis, K.-C., Hemleben, C., Schulz, H., Sperling, M., Weldeab,
 1037 S., 2003. Benthic foraminiferal record of ecosystem variability in the eastern Mediterranean
 1038 Sea during times of sapropel S5 and S6 deposition. *Palaeogeogr. Palaeoclimatol. Palaeoecol.*
 1039 190, 139–164. [https://doi.org/10.1016/S0031-0182\(02\)00603-X](https://doi.org/10.1016/S0031-0182(02)00603-X)
- 1040 Schmiidl, G., Pfeilsticker, M., Hemleben, C., Mackensen, A., 2004. Environmental and biological
 1041 effects on the stable isotope composition of recent deep-sea benthic foraminifera from the
 1042 western Mediterranean Sea. *Mar. Micropaleontol.* 51, 129–152.
 1043 <https://doi.org/10.1016/J.MARMICRO.2003.10.001>
- 1044 Schroeder, K., Garc a-Lafuente, J., Josey, S.A., Artale, V., Nardelli, B.B., Carrillo, A., Gacic, M.,
 1045 Gasparini, G. Pietro, Herrmann, M., Lionello, P., others, 2012. Circulation of the
 1046 Mediterranean Sea and its variability. *Clim. Mediterr. Reg. Ed. by Lionello, P., Elsevier* 187–
 1047 256.
- 1048 Scrivner, A.E., Vance, D., Rohling, E.J., 2004. New neodymium isotope data quantify Nile
 1049 involvement in Mediterranean anoxic episodes. *Geology* 32, 565.
 1050 <https://doi.org/10.1130/G20419.1>
- 1051 Shanahan, T.M., McKay, N.P., Hughen, K.A., Overpeck, J.T., Otto-Bliesner, B., Heil, C.W., King, J.,
 1052 Scholz, C.A., Peck, J., 2015. The time-transgressive termination of the African Humid Period.
 1053 *Nat. Geosci.* 8, 140–144. <https://doi.org/10.1038/ngeo2329>
- 1054 Siddall, M., Khatiwala, S., van de Flierdt, T., Jones, K., Goldstein, S.L., Hemming, S.R., Anderson,
 1055 R.F., 2008. Towards explaining the Nd paradox using reversible scavenging in an ocean
 1056 general circulation model. *Earth Planet. Sci. Lett.* 274, 448–461.
 1057 <https://doi.org/10.1016/j.epsl.2008.07.044>
- 1058 Sierro, F.J., Hodell, D.A., Curtis, J.H., Flores, J.A., Reguera, I., Colmenero-Hidalgo, E., B arcena, M.A.,
 1059 Grimalt, J.O., Cacho, I., Frigola, J., Canals, M., 2005. Impact of iceberg melting on
 1060 Mediterranean thermohaline circulation during Heinrich events. *Paleoceanography* 20, n/a-
 1061 n/a. <https://doi.org/10.1029/2004PA001051>
- 1062 Singh, S.P., Singh, S.K., Goswami, V., Bhushan, R., Rai, V.K., 2012. Spatial distribution of dissolved
 1063 neodymium and ϵNd in the Bay of Bengal: Role of particulate matter and mixing of water
 1064 masses. *Geochim. Cosmochim. Acta* 94, 38–56. <https://doi.org/10.1016/J.GCA.2012.07.017>
- 1065 Skonieczny, C., McGee, D., Winckler, G., Bory, A., Bradtmiller, L.I., Kinsley, C.W., Polissar, P.J., De
 1066 Pol-Holz, R., Rossignol, L., Malaiz e, B., 2019. Monsoon-driven Saharan dust variability over the
 1067 past 240,000 years. *Sci. Adv.* 5. <https://doi.org/10.1126/sciadv.aav1887>
- 1068 Skonieczny, C., Paillou, P., Bory, A., Bayon, G., Biscara, L., Crosta, X., Eynaud, F., Malaiz e, B., Revel,
 1069 M., Aleman, N., Barousseau, J.P., Vernet, R., Lopez, S., Grousset, F., 2015. African humid
 1070 periods triggered the reactivation of a large river system in Western Sahara. *Nat. Commun.* 6.

1071 <https://doi.org/10.1038/ncomms9751>

1072 Spivack, A.J., Wasserburg, G.J., 1988. Neodymium isotopic composition of the Mediterranean
1073 outflow and the eastern North Atlantic. *Geochim. Cosmochim. Acta* 52, 2767–2773.
1074 [https://doi.org/10.1016/0016-7037\(88\)90144-5](https://doi.org/10.1016/0016-7037(88)90144-5)

1075 Sprovieri, M., Di Stefano, E., Incarbona, A., Salvagio Manta, D., Pelosi, N., Ribera d’Alcalà, M.,
1076 Sprovieri, R., 2012. Centennial- to millennial-scale climate oscillations in the Central-Eastern
1077 Mediterranean Sea between 20,000 and 70,000 years ago: evidence from a high-resolution
1078 geochemical and micropaleontological record. *Quat. Sci. Rev.* 46, 126–135.
1079 <https://doi.org/10.1016/J.QUASCIREV.2012.05.005>

1080 Stratford, K., Williams, R.G., Myers, P.G., 2000. Impact of the circulation on sapropel formation in
1081 the eastern Mediterranean. *Global Biogeochemical Cycles* 14, 683–695.

1082 Tachikawa, K., Athias, V., Jeandel, C., 2003. Neodymium budget in the modern ocean and paleo-
1083 oceanographic implications. *J. Geophys. Res.* 108, 3254.
1084 <https://doi.org/10.1029/1999JC000285>

1085 Tachikawa, K., Piotrowski, A.M., Bayon, G., 2014. Neodymium associated with foraminiferal
1086 carbonate as a recorder of seawater isotopic signatures. *Quat. Sci. Rev.* 88, 1–13.
1087 <https://doi.org/10.1016/j.quascirev.2013.12.027>

1088 Tachikawa, K., Roy-Barman, M., Michard, A., Thouron, D., Yeghicheyan, D., Jeandel, C., 2004.
1089 Neodymium isotopes in the Mediterranean Sea: comparison between seawater and sediment
1090 signals. *Geochim. Cosmochim. Acta* 68, 3095–3106.
1091 <https://doi.org/10.1016/j.gca.2004.01.024>

1092 Tachikawa, K., Toyofuku, T., Basile-Doelsch, I., Delhaye, T., 2013. Microscale neodymium
1093 distribution in sedimentary planktonic foraminiferal tests and associated mineral phases.
1094 *Geochim. Cosmochim. Acta* 100, 11–23. <https://doi.org/10.1016/j.gca.2012.10.010>

1095 Tachikawa, K., Vidal, L., Cornuault, M., Garcia, M., Pothin, A., Sonzogni, C., Bard, E., Menot, G.,
1096 Revel, M., 2015. Eastern Mediterranean Sea circulation inferred from the conditions of S1
1097 sapropel deposition. *Clim. Past* 11, 855–867. <https://doi.org/10.5194/cp-11-855-2015>

1098 Tesi, T., Asioli, A., Minisini, D., Maselli, V., Valle, G.D., Gamberi, F., Langone, L., Cattaneo, A.,
1099 Montagna, P., Trincardi, F., 2017. Large-scale response of the Eastern Mediterranean
1100 thermohaline circulation to African monsoon intensification during sapropel S1 formation.
1101 *Quaternary Science Reviews* 159, 139–154.

1102 Thunell, R.C., Williams, D.F., 1989. Glacial–Holocene salinity changes in the Mediterranean Sea:
1103 hydrographic and depositional effects. *Nature* 338, 493–496.
1104 <https://doi.org/10.1038/338493a0>

1105 Toucanne, S., Jouet, G., Ducassou, E., Bassetti, M.A., Dennielou, B., Angue Minto’o, C.M., Lahmi,
1106 M., Touyet, N., Charlier, K., Lericolais, G., Mulder, T., 2012. A 130,000-year record of
1107 Levantine Intermediate Water flow variability in the Corsica Trough, western Mediterranean
1108 Sea. *Quat. Sci. Rev.* 33, 55–73. <https://doi.org/10.1016/j.quascirev.2011.11.020>

1109 Toucanne, S., Minto, C.M.A., Fontanier, C., Bassetti, M.A., Jorry, S.J., Jouet, G., 2015. Tracking
1110 rainfall in the northern Mediterranean borderlands during sapropel deposition. *Quaternary
1111 Science Reviews* 129, 178–195.

1112 Vadsaria, T., Ramstein, G., Dutay, J. -C., Li, L., Ayache, M., Richon, C., 2019. Simulating the
1113 Occurrence of the Last Sapropel Event (S1): Mediterranean Basin Ocean Dynamics
1114 Simulations Using Nd Isotopic Composition Modeling. *Paleoceanogr. Paleoclimatology* 34,
1115 237–251. <https://doi.org/10.1029/2019PA003566>

1116 Vance, D., Burton, K.W., 1999. Neodymium isotopes in planktonic foraminifera: a record of the
1117 response of continental weathering and ocean circulation rates to climate change. *Earth
1118 Planet. Sci. Lett.* 173, 365–379. [https://doi.org/10.1016/S0012-821X\(99\)00244-7](https://doi.org/10.1016/S0012-821X(99)00244-7)

- 1119 Vance, D., Scrivner, A.E., Beney, P., 2004. The use of foraminifera as a record of the past
1120 neodymium isotope composition of seawater. *Paleoceanography* 19, PA2009–PA2009.
1121 <https://doi.org/10.1029/2003PA000957>
- 1122 Wehausen, R., Brumsack, H.-J., 1999. Cyclic variations in the chemical composition of eastern
1123 Mediterranean Pliocene sediments: a key for understanding sapropel formation. *Mar. Geol.*
1124 153, 161–176. [https://doi.org/10.1016/S0025-3227\(98\)00083-8](https://doi.org/10.1016/S0025-3227(98)00083-8)
- 1125 Weldeab, S., Emeis, K.-C., Hemleben, C., Siebel, W., 2002a. Provenance of lithogenic surface
1126 sediments and pathways of riverine suspended matter in the Eastern Mediterranean Sea:
1127 evidence from $^{143}\text{Nd}/^{144}\text{Nd}$ and $^{87}\text{Sr}/^{86}\text{Sr}$ ratios. *Chem. Geol.* 186, 139–149.
1128 [https://doi.org/10.1016/S0009-2541\(01\)00415-6](https://doi.org/10.1016/S0009-2541(01)00415-6)
- 1129 Weldeab, S., Emeis, K.-C., Hemleben, C., Vennemann, T.W., Schulz, H., 2002b. Sr and Nd isotope
1130 composition of Late Pleistocene sapropels and nonsapropelic sediments from the Eastern
1131 Mediterranean Sea: implications for detrital influx and climatic conditions in the source areas.
1132 *Geochim. Cosmochim. Acta* 66, 3585–3598. [https://doi.org/10.1016/S0016-7037\(02\)00954-7](https://doi.org/10.1016/S0016-7037(02)00954-7)
- 1133 Williams, M.A., Adamson, D., Cock, B., McEvedy, R., 2000. Late Quaternary environments in the
1134 White Nile region, Sudan. *Glob. Planet. Change* 26, 305–316. [https://doi.org/10.1016/S0921-8181\(00\)00047-3](https://doi.org/10.1016/S0921-8181(00)00047-3)
- 1136 Wu, J., Böning, P., Pahnke, K., Tachikawa, K., de Lange, G.J., 2016. Unraveling North-African
1137 riverine and eolian contributions to central Mediterranean sediments during Holocene
1138 sapropel S1 formation. *Quat. Sci. Rev.* 152, 31–48.
1139 <https://doi.org/10.1016/J.QUASCIREV.2016.09.029>
- 1140 Wu, J., Liu, Z., Stuu, J.-B. Zhao, Y., Schirone, A., Lange G.-J., 2017. North-African paleodrainage
1141 discharges to the central Mediterranean during the last 18,000 years: A multiproxy
1142 characterization, *Quaternary Science Reviews* 163, 95–113
- 1143 Wu, J., Pahnke, K., Böning, P., Wu, L., Michard, A., de Lange, G.J., 2019. Divergent Mediterranean
1144 seawater circulation during Holocene sapropel formation – Reconstructed using Nd isotopes
1145 in fish debris and foraminifera. *Earth Planet. Sci. Lett.* 511, 141–153.
1146 <https://doi.org/10.1016/J.EPSL.2019.01.036>
- 1147 Wu, Q., Colin, C., Liu, Z., Douville, E., Dubois-Dauphin, Q., Frank, N., 2015a. New insights into
1148 hydrological exchange between the South China Sea and the Western Pacific Ocean based on
1149 the Nd isotopic composition of seawater. *Deep Sea Res. Part II Top. Stud. Oceanogr.* 122, 25–
1150 40. <https://doi.org/10.1016/j.dsr2.2015.11.005>
- 1151 Wu, Q., Colin, C., Liu, Z., Thil, F., Dubois-Dauphin, Q., Frank, N., Tachikawa, K., Bordier, L., Douville,
1152 E., 2015b. Neodymium isotopic composition in foraminifera and authigenic phases of the
1153 South China Sea sediments: Implications for the hydrology of the North Pacific Ocean over
1154 the past 25 kyr. *Geochemistry, Geophys. Geosystems* 16, 3883–3904.
1155 <https://doi.org/10.1002/2015GC005871>
- 1156 Xu, Z., Li, T., Colin, C., Clift, P.D., Sun, R., Yu, Z., Wan, S., Lim, D., 2018. Seasonal Variations in the
1157 Siliciclastic Fluxes to the Western Philippine Sea and Their Impacts on Seawater ϵ_{Nd} Values
1158 Inferred From 1 Year of In Situ Observations Above Benham Rise. *J. Geophys. Res. Ocean.* 123,
1159 6688–6702. <https://doi.org/10.1029/2018JC014274>
- 1160 Yu, Z., Colin, C., Ma, R., Meynadier, L., Wan, S., Wu, Q., Kallel, N., Sepulcre, S., Dapoigny, A.,
1161 Bassinot, F., 2018. Antarctic Intermediate Water penetration into the Northern Indian Ocean
1162 during the last deglaciation. *Earth Planet. Sci. Lett.* 500, 67–75.
1163 <https://doi.org/10.1016/J.EPSL.2018.08.006>
- 1164 Zhao, Y., Colin, C., Liu, Z., Paterne, M., Siani, G., Xie, X., 2012. Reconstructing precipitation changes
1165 in northeastern Africa during the Quaternary by clay mineralogical and geochemical
1166 investigations of Nile deep-sea fan sediments. *Quat. Sci. Rev.* 57, 58–70.

1167 <https://doi.org/10.1016/J.QUASCIREV.2012.10.009>
 1168 Zhao, Y., Liu, Z., Colin, C., Paterne, M., Siani, G., Cheng, X., Duchamp-Alphonse, S., Xie, X., 2011.
 1169 Variations of the Nile suspended discharges during the last 1.75 Myr. *Palaeogeogr.*
 1170 *Palaeoclimatol. Palaeoecol.* 311, 230–241. <https://doi.org/10.1016/J.PALAEO.2011.09.001>
 1171
 1172
 1173

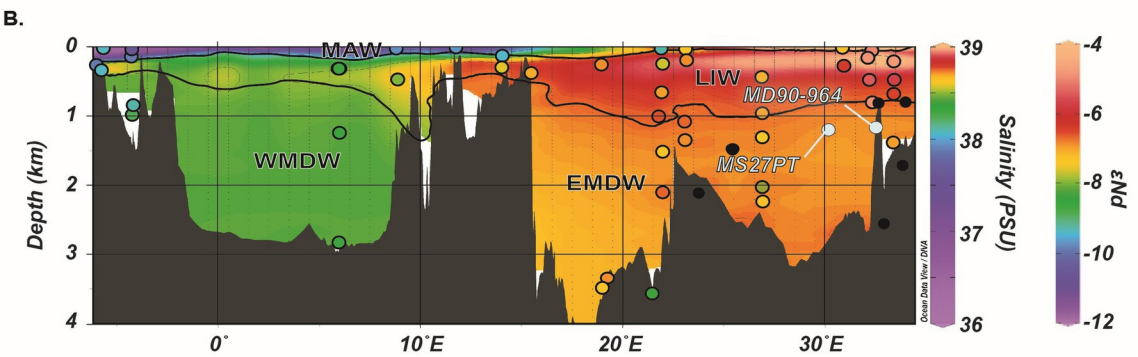
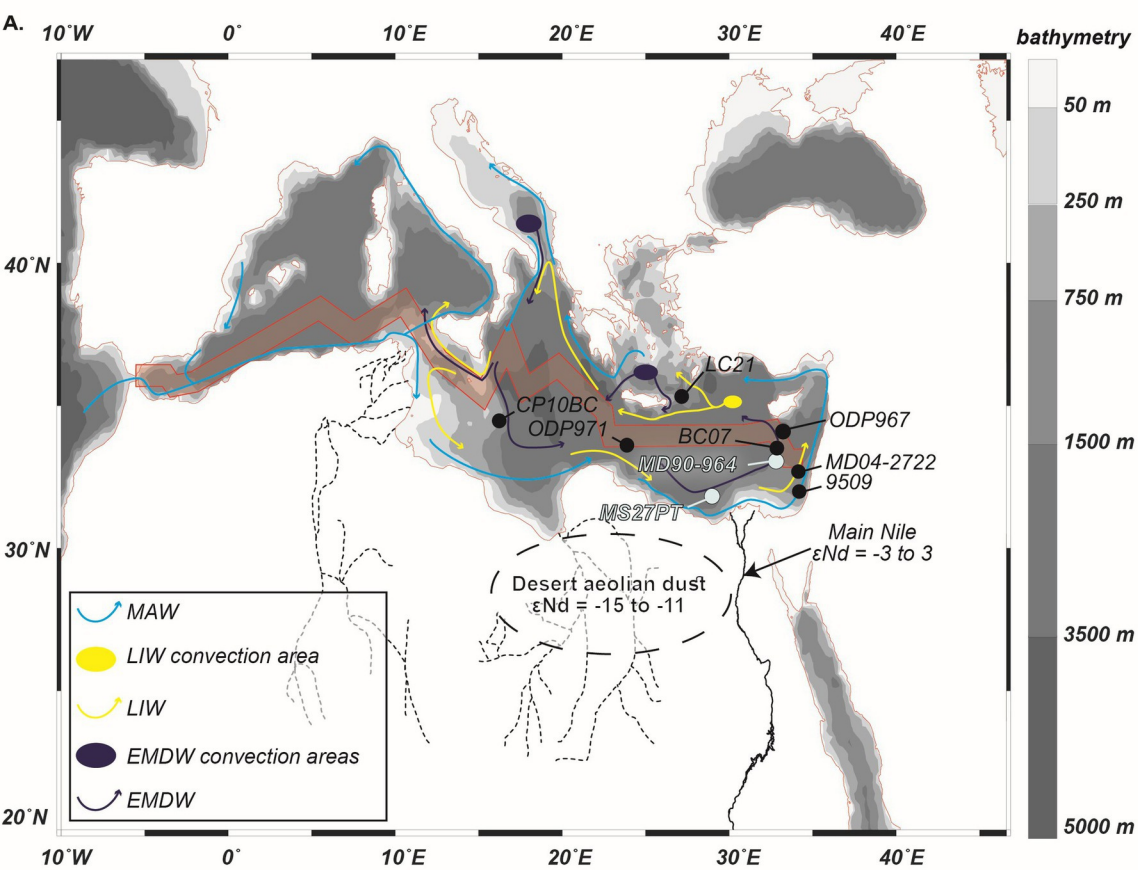
Depth (cm)	Age (cal kyr BP)	$^{143}\text{Nd}/^{144}\text{Nd}$	$\pm 2\sigma$	ϵNd	$\pm 2\sigma$	Samples
0.5	0.7	0.512432	± 0.000008	-4.03	± 0.17	uncleaned mixed planktonic foraminifera
2.5	1.3	0.512399	± 0.000008	-4.67	± 0.16	uncleaned mixed planktonic foraminifera
6	2.4	0.512345	± 0.000007	-5.71	± 0.13	cleaned mixed planktonic foraminifera
6	2.4	0.512351	± 0.000007	-5.61	± 0.13	cleaned <i>G. ruber</i>
6	2.4	0.512332	± 0.000018	-5.97	± 0.35	cleaning solution, mixed planktonic foraminifera
6	2.4	0.512335	± 0.000008	-5.91	± 0.15	uncleaned mixed planktonic foraminifera
9.5	3.0	0.512354	± 0.000010	-5.53	± 0.20	uncleaned mixed planktonic foraminifera
10	3.1	0.512357	± 0.000008	-5.49	± 0.16	cleaned mixed planktonic foraminifera
10	3.1	0.512360	± 0.000012	-5.42	± 0.23	uncleaned mixed planktonic foraminifera
10	3.1	0.512359	± 0.000007	-5.44	± 0.13	uncleaned mixed planktonic foraminifera
14.5	4.3	0.512358	± 0.000009	-5.46	± 0.18	uncleaned mixed planktonic foraminifera
18	5.1	0.512415	± 0.000014	-4.36	± 0.27	uncleaned mixed planktonic foraminifera
18	5.1	0.512430	± 0.000013	-4.06	± 0.25	uncleaned <i>G. ruber</i>
22	5.9	0.512417	± 0.000009	-4.31	± 0.18	uncleaned mixed planktonic foraminifera
29	6.9	0.512455	± 0.000011	-3.57	± 0.22	uncleaned <i>G. ruber</i>
95	8.7	0.512450	± 0.000012	-3.67	± 0.23	uncleaned mixed planktonic foraminifera
102	8.9	0.512471	± 0.000017	-3.26	± 0.33	uncleaned mixed planktonic foraminifera
102	8.9	0.512490	± 0.000015	-2.89	± 0.29	uncleaned <i>G. ruber</i>
120	9.1	0.512468	± 0.000009	-3.31	± 0.17	uncleaned mixed planktonic foraminifera
200	9.7	0.512498	± 0.000009	-2.72	± 0.18	uncleaned mixed planktonic foraminifera
205	9.8	0.512509	± 0.000011	-2.51	± 0.21	cleaned mixed planktonic foraminifera
205	9.8	0.512529	± 0.000008	-2.12	± 0.16	cleaning solution, mixed planktonic foraminifera
273	12.3	0.512452	± 0.000012	-3.63	± 0.23	uncleaned mixed planktonic foraminifera
280	12.7	0.512482	± 0.000013	-3.05	± 0.25	uncleaned mixed planktonic foraminifera
293	14.1	0.512450	± 0.000009	-3.66	± 0.17	cleaned mixed planktonic foraminifera
293	14.1	0.512474	± 0.000007	-3.20	± 0.14	cleaned <i>G. ruber</i>
293	14.1	0.512459	± 0.000023	-3.49	± 0.44	cleaning solution, mixed planktonic foraminifera
293	14.1	0.512483	± 0.000017	-3.02	± 0.34	cleaning solution, <i>G. ruber</i>
299	16.4	0.512398	± 0.000010	-4.68	± 0.19	uncleaned mixed planktonic foraminifera
303	20.6	0.512390	± 0.000007	-4.83	± 0.14	cleaned mixed planktonic foraminifera
303	20.6	0.512386	± 0.000007	-4.91	± 0.14	cleaned mixed planktonic foraminifera
315	25.8	0.512411	± 0.000007	-4.44	± 0.13	cleaned <i>G. ruber</i>

Table 1

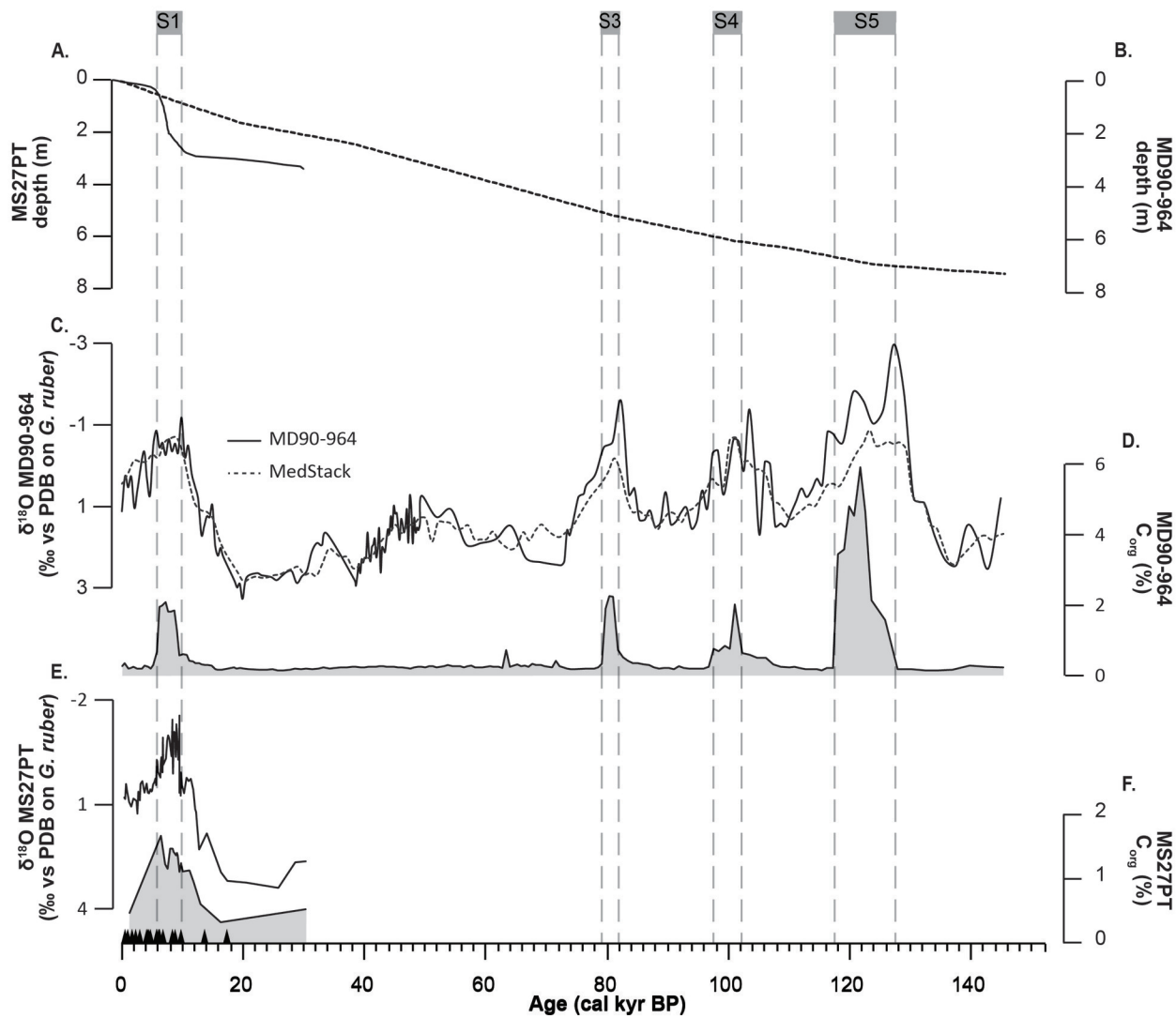
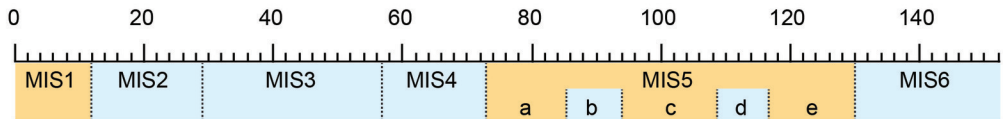
Depth (cm)	Age (kyr)	$^{143}\text{Nd}/^{144}\text{Nd}$	$\pm 2\sigma$	ϵNd	$\pm 2\sigma$
4	0.5	0.512441	± 0.000011	-3.84	± 0.21
8	0.9	0.512413	± 0.000009	-4.39	± 0.18
16	1.9	0.512410	± 0.000008	-4.45	± 0.17
28	3.3	0.512410	± 0.000011	-4.45	± 0.21
40	4.7	0.512438	± 0.000010	-3.89	± 0.19
52	6.2	0.512454	± 0.000010	-3.58	± 0.19
72	8.5	0.512450	± 0.000011	-3.66	± 0.22
80	9.5	0.512457	± 0.000009	-3.53	± 0.18
108	13.2	0.512476	± 0.000009	-3.17	± 0.18
128	15.8	0.512430	± 0.000010	-4.07	± 0.19
152	19.0	0.512464	± 0.000009	-3.40	± 0.18
160	20.0	0.512462	± 0.000010	-3.43	± 0.19
172	22.8	0.512537	± 0.000009	-1.96	± 0.17
200	29.5	0.512470	± 0.000008	-3.27	± 0.15
224	35.2	0.512483	± 0.000008	-3.03	± 0.16
236	38.0	0.512462	± 0.000010	-3.43	± 0.19
280	45.0	0.512478	± 0.000010	-3.12	± 0.19
304	48.8	0.512474	± 0.000010	-3.20	± 0.20
324	51.9	0.512473	± 0.000009	-3.22	± 0.18
380	60.8	0.512497	± 0.000011	-2.75	± 0.21
384	61.4	0.512483	± 0.000009	-3.02	± 0.18
420	67.1	0.512484	± 0.000010	-3.00	± 0.19
452	72.1	0.512442	± 0.000010	-3.82	± 0.20
484	77.2	0.512430	± 0.000010	-4.06	± 0.20
504	80.4	0.512440	± 0.000008	-3.85	± 0.16
512	81.8	0.512456	± 0.000007	-3.55	± 0.15
524	84.3	0.512459	± 0.000008	-3.50	± 0.16
556	91.0	0.512412	± 0.000008	-4.42	± 0.15
580	96.0	0.512453	± 0.000010	-3.60	± 0.20
592	98.5	0.512455	± 0.000009	-3.58	± 0.18
596	99.3	0.512484	± 0.000010	-3.00	± 0.19
600	100.2	0.512462	± 0.000011	-3.42	± 0.22
604	101.0	0.512469	± 0.000009	-3.30	± 0.18
608	102.3	0.512495	± 0.000015	-2.79	± 0.29
628	108.7	0.512439	± 0.000009	-3.88	± 0.17
632	110.0	0.512331	± 0.000008	-5.99	± 0.39
636	110.9	0.512454	± 0.000009	-3.59	± 0.16
652	114.5	0.512431	± 0.000016	-4.03	± 0.18
656	115.4	0.512432	± 0.000010	-4.01	± 0.32
660	116.3	0.512421	± 0.000009	-4.23	± 0.19
664	117.2	0.512427	± 0.000008	-4.12	± 0.17
668	118.1	0.512415	± 0.000009	-4.35	± 0.16

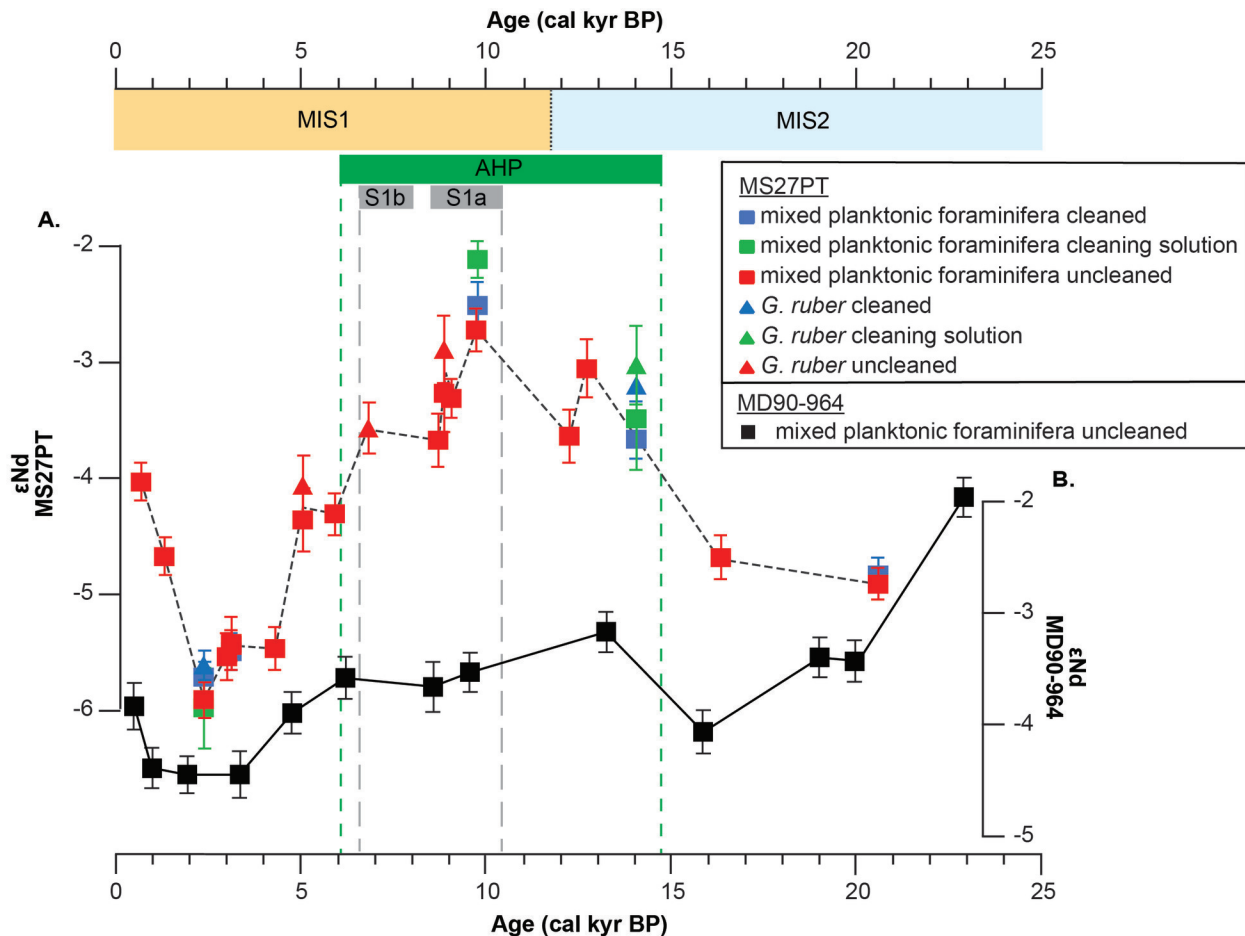
672	119.0	0.512397	± 0.000010	-4.70	± 0.17
676	119.9	0.512420	± 0.000010	-4.25	± 0.20
680	120.8	0.512405	± 0.000011	-4.54	± 0.20
684	121.7	0.512429	± 0.000009	-4.07	± 0.22
688	122.6	0.512436	± 0.000009	-3.94	± 0.17
692	123.5	0.512429	± 0.000013	-4.07	± 0.18
700	128.0	0.512399	± 0.000011	-4.66	± 0.24
704	130.3	0.512421	± 0.000009	-4.23	± 0.21
708	132.5	0.512418	± 0.000012	-4.29	± 0.18
712	134.8	0.512446	± 0.000013	-3.75	± 0.23
716	137.0	0.512483	± 0.000008	-3.02	± 0.26
720	139.8	0.512448	± 0.000009	-3.71	± 0.16
728	145.4	0.512454	± 0.000011	-3.59	± 0.17

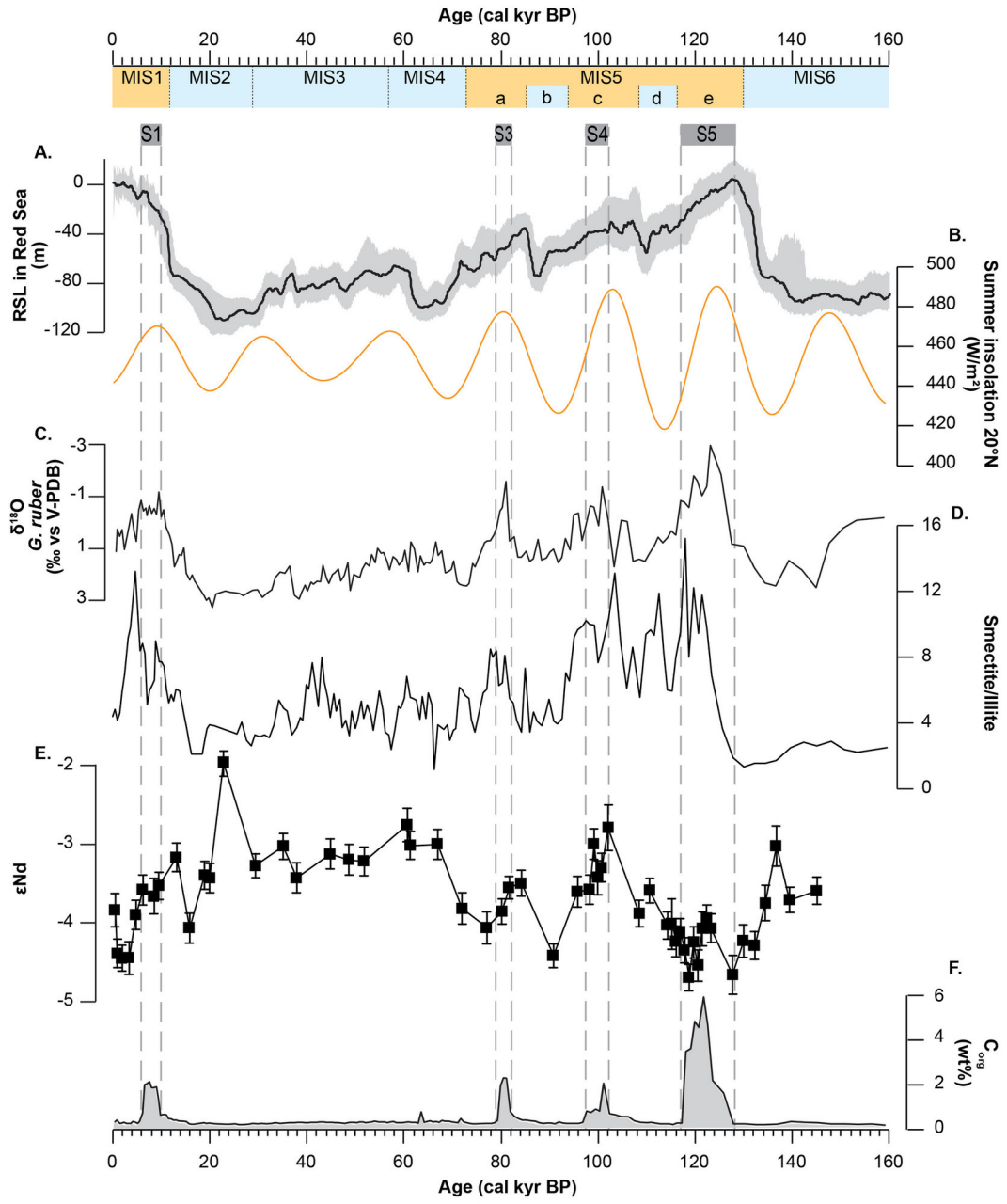
Table 2



Age (cal kyr BP)







Age (cal kyr BP)

0 5 10 15 20 25

MIS1

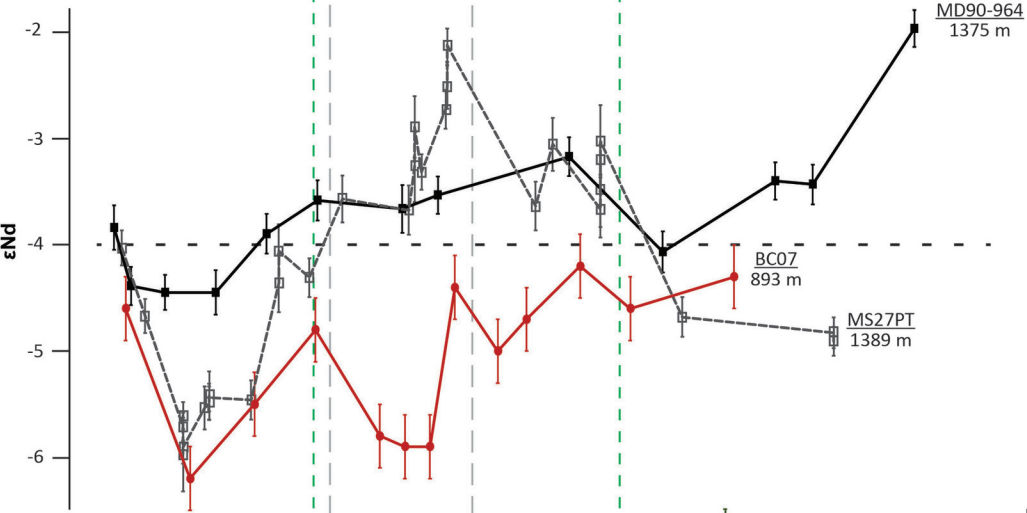
MIS2

AHP

S1b

S1a

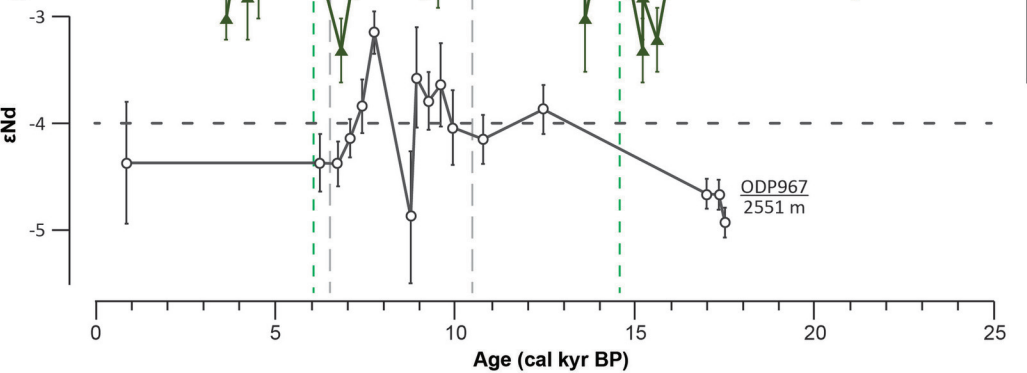
A.



B.

$\delta^{13}C$

C.



MD04-2722
1780 m

ODP967
2551 m

Age (cal kyr BP)

0 5 10 15 20 25

